SÃO PAULO STATE UNIVERSITY
Graduate Program in Mechanical Engineering
Campus Bauru

Piezoelectric Nonlinear Energy Sink for Energy Harvesting in Aeroelastic System in Flutter Condition

Ana Carolina Godoy Amaral

Bauru

2026

Piezoelectric Nonlinear Energy Sink for Energy Harvesting in Aeroelastic System in Flutter Condition

Ana Carolina Godoy Amaral

Thesis presented at São Paulo State University, School of Engineering of Bauru, Postgraduate Program in Mechanical Engineering in the Area of Mechanical Projects, as part of the requirements necessary to obtain the title of Doctor of Mechanical Engineering.

Supervisor: Prof. Dr. Fabricio Cesar Lobato de Almeida

Bauru
2026

A485p

Amaral, Ana Carolina Godoy
Piezoelectric Nonlinear Energy Sink for Energy Harvesting in Aeroelastic System in Flutter Condition / Ana Carolina Godoy Amaral. -- Bauru, 2026
102 p. : il., tabs.

Tese (doutorado) - Universidade Estadual Paulista (UNESP), Faculdade de Engenharia, Bauru
Orientador: Fabricio Cesar Lobato de Almeida

1. Piezoeletric nonlinear energy sink. 2. Energy harvesting. 3. Flutter. 4. Uncertainty analysis. I. Título.

UNIVERSIDADE ESTADUAL PAULISTA

Câmpus de Bauru

ATA DA DEFESA PÚBLICA DA TESE DE DOUTORADO DE ANA CAROLINA GODOY AMARAL, DISCENTE DO PROGRAMA DE PÓS-GRADUAÇÃO EM ENGENHARIA MECÂNICA, DA FACULDADE DE ENGENHARIA - CÂMPUS DE BAURU.

Aos 03 de fevereiro de 2026, às 9h, por meio de Videoconferência, realizou-se a defesa de TESE DE DOUTORADO de ANA CAROLINA GODOY AMARAL, intitulada "Piezoelectric Nonlinear Energy Sink for Energy Harvesting in Aeroelastic System in Flutter Condition". A Comissão Examinadora foi constituída pelos seguintes membros: Prof. Dr. FABRICIO CESAR LOBATO DE ALMEIDA (Orientador(a) - Participação Virtual) do(a) Departamento de Engenharia Mecânica / UNESP / Câmpus de Bauru - FEB, Prof. Dr. FABIO MAZZARIOL SANTICIOLLI (Participação Virtual) do(a) Departamento de Engenharia Mecânica / UNESP / Câmpus de Bauru - FEB, Prof. Dr. DOUGLAS DOMINGUES BUENO (Participação Virtual) do(a) Departamento de Engenharia Mecânica / UNESP / Câmpus de Ilha Solteira - FEIS, Prof. Dr. WIM DE ROECK (Participação Virtual) do(a) Katholieke Universiteit Leuven, Prof. Dr. LUIS GUSTAVO GIACON VILLANI (Participação Virtual) do(a) Departamento de Engenharia Mecânica / Universidade Federal do Espírito Santo (UFES), Após a exposição pela doutoranda e arguição pelos membros da Comissão Examinadora que participaram do ato, de forma presencial e/ou virtual, a discente recebeu o conceito final: APROVADA _ _ _ _ _ _ _ _ _ _ _ _ _ . Nada mais havendo, foi lavrada a presente ata, que após lida e aprovada, foi assinada pelo(a) Presidente(a) da Comissão Examinadora.

Documento assinado digitalmente
gov.br FABRICIO CESAR LOBATO DE ALMEIDA
Data: 19/02/2026 09:39:40-0300
Verifique em https://validar.iti.gov.br

Prof. Dr. FABRICIO CESAR LOBATO DE ALMEIDA

Acknowledgements

This study was funded by the Coordination for the Improvement of Higher Education Personnel (CAPES), process number 88887.606139/2021-00 and process number 88881.846223/2023-01). I would like do express my heartfelt thanks to the following: UNESP, for providing and enriching environment that fostered my academic growth and development. My supervisors, Professor Marcos Silveira and Fabricio Lobato de Almeida, for their encouragement, dedication, patience, and the knowledge shared throughout the development of this work. I am also grateful to my family and to the NDE research group for all the support and encouragement during this period.

Piezoelectric Nonlinear Energy Sink for Energy Harvesting in Aeroelastic System in Flutter Condition

Ana Carolina Godoy Amaral

Abstract This work presents a comprehensive analysis of an aeroelastic system in flutter conditions and with a Piezoelectric Nonlinear Energy Sink (PNES). A nonlinear energy sink (NES) is a nonlinear absorber, typically implemented as a secondary mechanical system designed as a passive absorber. The PNES is an NES that integrates a piezoelectric component, thereby enabling it to also function as an energy harvester useful for powering autonomous systems. The research spanned three main stages: model validation, energy harvesting performance, and robustness assessment. The model validation was performed by comparing the low order model using Dowell aerodynamics (LOM-Dowell model) against a multibody model with computational fluid dynamics simulations (multibody-CFD model). The energy harvesting performance analysis used the Multiple Scales Method (MMS) and Runge-Kutta simulation (RK). The cubic nonlinear stiffness coefficient (δ) was found to increase flutter speed (U^*) at the expense of reducing system response and harvested electrical power (P_e). Conversely, the quadratic nonlinear electromechanical coupling coefficient (K) increases P_e. Finally, a probabilistic uncertainty analysis, employing Monte Carlo Simulation (MCS), assessed system robustness. The uncertainty analysis established the superior robustness of the nonlinear PNES system compared to the linear configuration. The analysis also confirmed that the electromechanical coupling (θ) and plunge stiffness (k_h) are the dominant parameters influencing power output under uncertainty. In conclusion, the PNES not only increases energy harvesting but also enhances the system's robustness, resulting in a more reliable power output than its linear counterpart.

Keywords: piezoelectric nonlinear energy sink, energy harvesting,
flutter, uncertainty analysis

Piezoelectric Nonlinear Energy Sink para Energy Harvesting em seção aeroelástica em Condição de Flutter

Ana Carolina Godoy Amaral

Resumo Este trabalho apresenta uma análise de um sistema aeroelástico em condições de flutter com um Piezoelétrico Nonlinear Energy Sink (PNES). Um Nonlinear Energy Sink (NES) é um absorvedor não linear, geralmente implementado como um sistema mecânico secundário projetado para absorção passiva. O PNES é um NES que integra um componente piezoelétrico, permitindo-lhe funcionar, também, como um energy harvester, útil para alimentar sistemas autónomos. A pesquisa abrangeu três etapas principais: validação do modelo, desempenho do energy harvesting e avaliação da robustez. A validação do modelo foi realizada comparando o modelo de baixa ordem utilizando a aerodinâmica de Dowell (modelo LOM-Dowell) com um modelo multibody com simulações de dinâmica de fluidos computacional (modelo multibody-CFD). A análise de energy harvesting utilizou o Método das Múltiplas Escalas (MMS) e simulação de Runge-Kutta (RK). Observou-se que o coeficiente de rigidez não linear cúbica (δ) aumenta a velocidade de flutter (U^*) à custa da redução da resposta do sistema e da potência elétrica coletada (P_e). Por outro lado, o coeficiente de acoplamento eletromecânico não linear quadrático (K) aumenta a P_e. Finalmente, uma análise probabilística de incerteza, empregando a Simulação de Monte Carlo (MCS), avaliou a robustez do sistema. A análise de incerteza estabeleceu a robustez superior do sistema PNES não linear em comparação com a configuração linear. A análise também confirmou que o acoplamento eletromecânico (θ) e a rigidez de plunge (k_h) são os parâmetros dominantes que influenciam a saída de potência sob incerteza. Em conclusão, o PNES não apenas aumenta a coleta de energia, mas também melhora a robustez do sistema, resultando em uma saída de potência mais confiável do que sua contraparte linear.

Keywords: piezoelétrico nonlinear energy sink, energy harvesting,
flutter, análise de incerteza

List of Figures

List of Tables

List of Symbols

Designation	Explanation
Latin symbols	
A	matrix of the main system for multiple scales
a	system response for the multiple scales method
A_d	area under power velocity curve for dashed lines
A_p	area under power velocity curve for pointed lines
A_s	area under power velocity curve for sharp lines
B	matrix that contains σ_u
b	semichord length
$\tilde{B}$	structural matrix of damping
bx_α	distance between elastic axis and centroid
C	centroid
c	chord length
C_c	cubic nonlinear vector
c_c	critical damping
C_e	damping matrix of the electrical damper
C_m	damping matrix of the mechanical damper
c_{ot}	optimum ratio between damper damping and critical damping
C_p	equivalent capacitance
c_1	damping of the main system

c_2	damping of the damper
D	aerodynamic matrix
d_h	damping coefficient for plunge
D_n	derivative time
d_α	damping coefficient for pitch
e	distance between aerodynamic center and elastic axis
E_1, E_2, F	aerodynamic matrix
f	frequency ration
F_1	Applied Force in the system
f_{ot}	optimum frequency
g	forced frequency ratio
h	plunge degree of freedom
I	identity matrix
I_α	moment of inertia
j	imaginary unit
K	quadratic nonlinear electromechanical coupling
$\tilde{K}$	structural matrix of stiffness
K_e	stiffness matrix of the electrical damper
k_h	damping coefficient for plunge
K_m	stiffness matrix of the mechanical damper
k_α	damping coefficient for pitch
k_1	stiffness of the main system
k_2	stiffness of the damper
L	inductance
L_h	lift force
m	airfoil mass
$\tilde{M}$	structural matrix of mass

M_e	mass matrix of the electrical damper
m_e	fixture mass
M_m	mass matrix of the mechanical damper
M_α	moment force
m_1	mass of the main system
m_2	mass of the damper
O	elastic axis
p	right eigenvector
P_e	transient average power
$\overline{P_e}$	steady-state average power per cycle
P_{ei}	instantaneous electric power
q	electric charge
q_q	left eigenvector
Q	quadratic nonlinear vector
R	electric resistance
R_n	indicator of the sensitivity of P_e
U	airflow velocity
U^*	flutter velocity
x_{st}	static deflection
x_1	variable of the main system
X_1	variable of the main system in frequency domain
x_2	variable of the damper
X_2	variable of the damper in frequency domain
Greek symbols	
α	pitch degree of freedom
β	multiple scales parameter
δ	cubic nonlinear stiffness coefficient

ϵ	small dimensionless parameter
ζ_0, ζ_2	multiple scales parameter
Θ	electromechanical coupling
Λ_a	multiple scales parameter
λ_i	coefficient of variation for input
μ	mass ratio
μ_n	deterministic nominal value
ρ	is the air density
σ	standard deviation
σ_u	dimensionless parameter to expand U_f
ω	frequency for one-degree-of-freedom system
ω_h	uncoupled natural frequency for plunge
ω_n	natural frequency for one-degree-of-freedom system
ω_α	uncoupled natural frequency for pitch
ω_2	damper frequency for one-degree-of-freedom system

Contents

Chapter 1

Introduction

The primary objective of energy harvesting is to capture the mechanical energy present in the environment (originating from the movement of objects, the vibration of structures, or human motion) and convert it into electrical power to supply electronic devices, such as remote sensors or transmitters. The practical implementation of energy harvesting spans a wide array of technological fields, ranging from large-scale structural monitoring to delicate biomedical devices. In the realm of structural and aerospace engineering, energy can be scavenged from the vibrations of bridge cables, the aerodynamic flow over winglets, or the oscillation of air conditioner vanes. These harvested sources are primarily used to power wireless sensors and microelectromechanical systems (MEMS), reducing the reliance on small batteries that require frequent replacement. Furthermore, this technology supports the operation of actuators and low-power consumer electronics, such as cellphones, while offering life-saving potential in the medical sector by providing a sustainable power source for pacemakers.

Energy harvesting devices, or harvesters, can benefit significantly from incorporating nonlinear properties, particularly for applications requiring effective operation across a broad range of excitation frequencies. One such device that leverages nonlinearity is the Nonlinear Energy Sink (NES). NESs utilize mechanical substructures with nonlinear characteristics, originally developed for the suppression of vibrations across a wide bandwidth.

A common and efficient type of energy harvester is the one that utilizes piezoelectric materials to convert mechanical energy into electrical energy. Piezoelectric components often exhibit nonlinear characteristics. Therefore, NESs can be designed as electromechanical systems by incorporating these materials. This integrated technology, capable of both vibration suppression and energy harvesting, is herein defined as a Piezoelectric Nonlinear Energy Sink (PNES).

Making the use of energy harvesting technology viable represents a major challenge, as the energy required to maintain electronic device operation is often greater than the energy extracted. While linear absorbers are capable of absorbing a reasonable amount of energy, their effectiveness is restricted to a single frequency. This limitation underscores the necessity of applying PNES technology, which has the potential to absorb a greater amount of electrical energy and operate across a wider range of frequencies compared to a similar linear absorber.

In the domain of aeroelasticity, the flutter phenomenon constitutes a source of vibration of particular interest, providing the necessary oscillatory motion for energy collection. This work discusses the response of a PNES used for the dual function of vibration suppression and energy harvesting in an aeroelastic typical section subjected to flutter. The main application is the development of small-scale aeroelastic harvesters for powering low-power electronic devices. Furthermore, the advantages and robustness of the PNES are analyzed in comparison to a similar linear absorber.

Figure 1.1 illustrates a conceptual framework linking the central themes of this work.

1.1 Energy harvesting in aeroelastic systems

Energy harvesters are precisely designed to extract energy from ambient vibration and subsequently transfer it to electrical devices available (Bibo and Daqaq, 2013; Safaei et al., 2019). The fundamental concept of energy harvesting, whether derived from

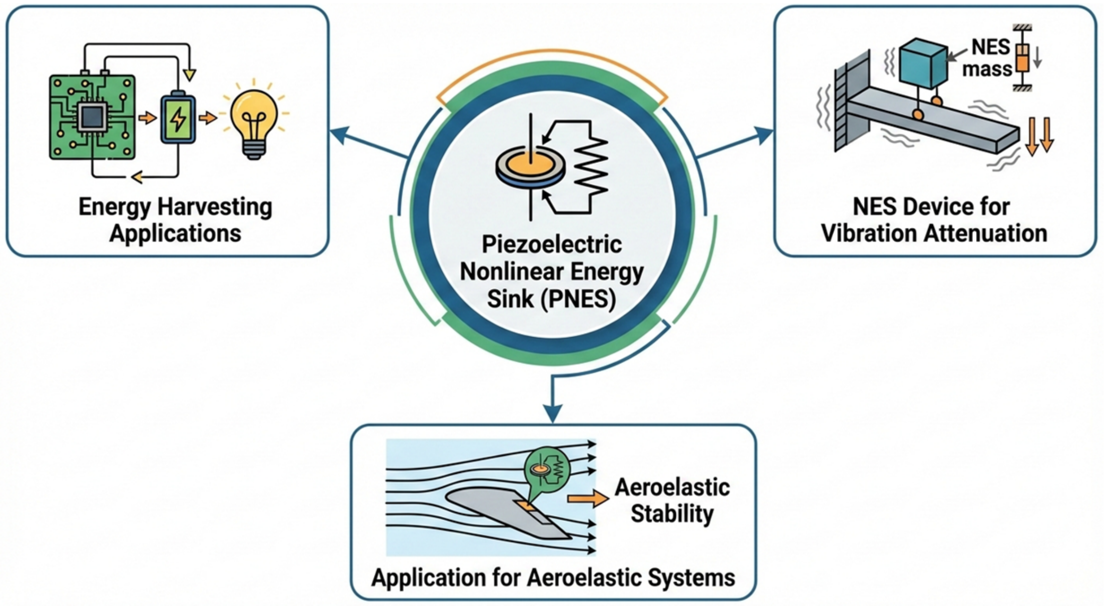

Figure 1.1: The main aspects of the PNES concept.

the environment or from the movements of living beings, dates back to 1880 with the foundational discovery of piezoelectricity by Pierre and Jacques Curie. Since then, the sustained interest in this energy source has driven the emergence of diverse technologies and research areas, including Micro Electromechanical Systems (MEMS), wireless sensors, work capturing energy from human movements, capturing energy from a voltage restriction system, in addition to several other ways of acquiring more energy. Similarly, the energy transducers employed are diverse, requiring varied techniques for energy capture, storage, and distribution, such as vibrational, radio frequency and thermal sources. Given the broad range of study areas and the challenge of establishing universal performance metrics, detailed investigation into specific, high-efficiency harvesting solutions, remains essential for making this form of energy viable for widespread device use (Harb, 2011).

A variety of energy harvesting technologies are currently being explored, including electromagnetic, piezoelectric, thermoelectric, pyroelectric, photovoltaic, and solar heat collectors (Petrescu et al., 2016; Wei and Jing, 2017). Figure 1.2 illustrates a specific example: a piezoelectric membrane transducer utilized for investigating the extraction of electrical energy from mechanical vibration (Ericka et al., 2005). Given its capacitance in converting mechanical deformation into electrical power, piezoelectric energy harvesting is the specific technology employed and investigated in this work.

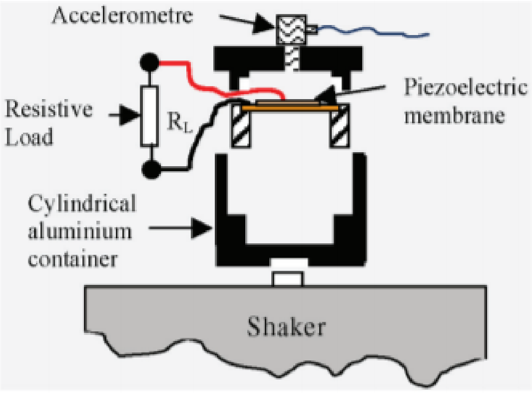

Figure 1.2: Energy harvesting from vibration using a piezoelectric membrane. Source: Ericka et al. (2005)

.

An important application for energy harvesting technology is in MEMS, which are capable of capturing vibrational energy from the ambient environment. Smart sensors utilizing this technique can maintain the level of extracted energy at its maximum capacity, thereby ensuring continuous operation and enabling auxiliary functions, such as data transmission. To ensure that the system captures the maximum possible power, it is critical to understand the variables governing the power output. These variables include the amplitude of the base motion or force, the magnitude of the applied force, and the excitation frequency. Consequently, MEMS harvesters must be designed with the capability to adapt to these changing environmental variables, often through the modification of the damping coefficient, to consistently extract the maximum possible power. These devices are particularly valuable for deployment in hostile environments where periodic battery replacement is impractical. After energy is extracted from the environment, it must be effectively deposited into electrical loads, a process that is significantly dependent on the system's electrical characteristics, primarily the internal resistance of the coil (Stephen, 2006).

It is evident that extracting the maximum output power is paramount to enhancing the commercial viability of energy harvesting technology. One effective approach to maximizing this power output involves the judicious selection of the piezoelectric material type and the optimal combination of system parameters (Kang et al., 2016). The study by Yang et al. (2017) discusses the efficiency of piezoelectric harvesters, noting that efficiency is primarily governed by the electromechanical coupling effect, the damping effect, the excitation frequency, and the electrical load. Therefore, a universal formula for maximizing output power does not exist, as the performance of each piezoelectric energy harvester is intrinsically linked to its unique set of parameters. This work addresses this performance challenge by aiming to increase the energy harvesting capability of the system through the inclusion of nonlinear elements and the specific design of the piezoelectric transducer as a PNES.

Energy harvesting can be seen as a means to attenuate, control or retard typical aeroelastic phenomena, such as flutter (Tsushima and Su, 2017), galloping (Jung and Lee, 2011; Abdelkefi et al., 2012a) and VIV (vortex induced vibrations) (Zhang et al., 2017a). A critically important topic in aeroelasticity is flutter, an undesirable phenomenon that occurs when an aircraft component exhibits a divergent oscillatory self-sustained behaviour upon reaching a specific velocity. This aeroelastic instability can lead to catastrophic structural damage (Jonsson et al., 2019). Experimental tests conducted in a wind tunnel constitute a crucial method for studying the flutter phenomenon (Marqui Jr et al., 2006). However, conducting extensive experimental tests on aeroelastic systems is often impractical due to the substantial space requirements and associated high costs. Consequently, simplified mathematical models of aeroelastic typical sections are frequently employed as a cost-effective alternative for investigation (Papatheou et al., 2012; Amaral et al., 2023; Lee et al., 2007b). Figure 1.3 represents the model of an airfoil under wind excitation with a piezoelectric transduction for energy harvesting.

Another approach for investigating aeroelastic systems can involve Computational

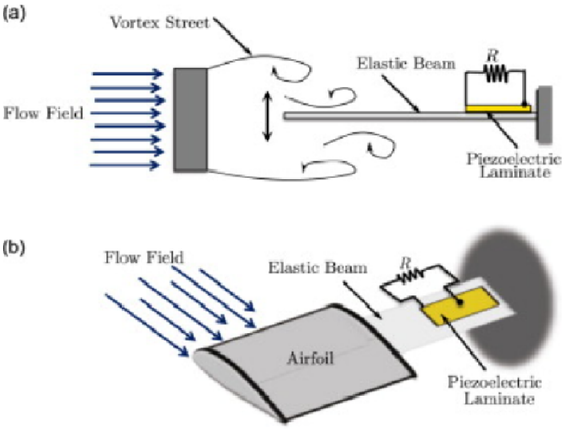

Figure 1.3: Piezoelectric harvester (a) Vortex street induced oscillations and (b) Flutter induced oscillations. Source: Bibo and Daqaq (2013)

.

Fluid Dynamics (CFD) software to describe aerodynamics. These numerical simulations are expected to yield responses that more closely approximate real-world behavior compared to simplified models. Previous work has successfully investigated the influence of structural parameters, such as airfoil stiffness, on flutter velocity using CFD solvers like STAR-CCM+ (Tylén, 2022).

The oscillatory movement caused by the flutter phenomenon constitutes an interesting source for research and study regarding energy harvesting. The combination of energy harvesting with vibration control in aeroelastic systems yields a dual benefit: it can increase the critical flutter velocity by suppressing the amplitude of vibration and it allows the production of electrical power, which can be directed to the aircraft's electronic devices (Tsushima and Su, 2017; Marqui Jr and Marques, 2005; Li et al., 2022).

1.2 Nonlinear energy sink (NES)

The necessity of absorbing and dissipating vibration energy in engineering systems is a long-standing challenge. Early foundational work, such as that by Nayfeh and Nayfeh

(1994), demonstrated interest in the transfer of energy between low- and high-frequency modes, a phenomenon stemming from modal instability. In the last two decades, the drive toward autonomous and self-powered systems has significantly intensified the demand for reliable energy harvesting technologies. This surge has further promoted the investigation into the benefits offered by nonlinear terms in both vibration control and energy harvesting applications (Erturk and Inman, 2011; Covaci and Gontean, 2020; Zheng et al., 2023).

Despite its widespread use and established performance, the linear dynamic vibration absorber possesses inherent limitations. Specifically, its optimal performance is restricted to a very narrow frequency band, a constraint that motivates the development of more robust, broadband solutions.

The damped linear dynamic vibration absorber, also known as a Tuned Mass Damper (TMD) or Dynamic Vibration Absorber (DVA), is a classical device utilized to attenuate the vibration of a structure over a specific frequency range. This device is formed by a secondary system coupled to the primary system (the structure) and it is responsible for absorbing vibration energy. For optimal operation, the natural frequency of the resulting coupled system must be detuned from the main excitation frequency and that is a significant limitation. The DVA is highly effective only within a narrow band of frequencies centered around the resonance condition for which it was tuned (Rao and Yap, 2011). If the primary system is required to operate over a wide range of excitation frequencies (a broadband response), the vibration amplitudes outside the tuned resonance region can remain excessively high. This frequency-dependent limitation is the primary driver for investigating advanced vibration mitigation technologies.

The one-degree-of-freedom mechanical system with damped mechanical linear absorber is represented by fig. 1.4 and eq. (1.1).

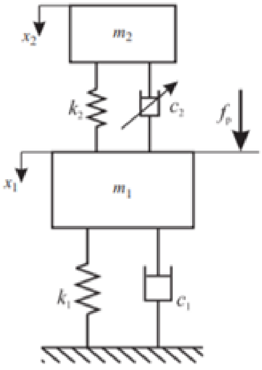

Figure 1.4: Damped linear dynamic vibration absorber coupled to one-degree-of-freedom mechanical system. Source: Jiang et al. (2003)

$$
\begin{aligned}
m_1\ddot{x}_1 + c_1\dot{x}_1 + k_1x_1 + k_2(x_1 - x_2) + c_2(\dot{x}_1 - \dot{x}_2) &= F_1 \sin \omega t \\
m_2\ddot{x}_2 + k_2(x_2 - x_1) + c_2(\dot{x}_2 - \dot{x}_1) &= 0 \qquad (1.1)
\end{aligned}
$$

in which m_1 is the mass of primary system, c_1 is the damping of primary system, k_1 is the stiffness of primary system, m_2 is the mass of absorber, c_2 is the damping of absorber and k_2 is the stiffness of absorber, x_1 is the degree of freedom of main system and x_2 is the degree of freedom of absorber.

The equations in 1.1, in the frequency domain, are presented by:

$$
\begin{aligned}
\left[-m_1\omega^2 + k_1 + j\omega c_1 + k_2 + j\omega c_2\right] X_1 - \left[k_2 + j\omega c_2\right] X_2 &= F_1 \qquad (1.2) \\
-\left[k_2 + j\omega c_2\right] X_1 + \left[-m_2\omega^2 + k_2 + j\omega c_2\right] X_2 &= 0
\end{aligned}
$$

The frequency response is given by:

$$\frac{X_1}{F_1} = \frac{[-m_2\omega^2 + k_2 + j\omega c_2]}{[-m_1\omega^2 + k_1 + j\omega c_1 + k_2 + j\omega c_2]\,[-m_2\omega^2 + k_2 + j\omega c_2] - [k_2 + j\omega c_2]^2} \tag{1.3}$$

To facilitated the resolution, it is considered $c_1 = 0$. Also, it is considered X_1/x_{st} equal the reason of amplitude of the main system mass as function of main parameters μ, c_2/c_c, f e g:

$$\frac{X_1}{x_{st}} = \sqrt{\frac{\left(2\frac{c_2}{c_c}g\right)^2 + \left(g^2 - f^2\right)^2}{\left(2\frac{c_2}{c_c}g\right)^2 \left(g^2 - 1 + \mu g^2\right)^2 + \left[\mu f^2 g^2 - \left(g^2 - 1\right)\left(g^2 - f^2\right)\right]^2}} \tag{1.4}$$

in which μ is the mass ratio, ω_2 is the damper natural frequency, ω_n is the main system natural frequency, f is the frequency ratio, g is the forced frequency ratio, x_{st} is the static deflection of the system, c_c is the critical damping.

The damper attached to the main system decreases the resonance peak of frequency response until an optimum value. Figure 1.5 shows the damper influence in the amplitude ratio. If $c_2/c_c = 0$, the system has no damping. If $c_2/c_c = 0.1$, the peaks decrease the amplitude. If $c_2/c_c = 0.3$, the peaks has a bigger amplitude decrease. If $c_2/c_c = 10$, the damper does not work, it works as a mass attached to the main system. Therefore, the damper works until an optimum value of c_2/c_c.

To find the optimum damper, in which the peaks have the minimum value possible, it is used two points P and Q. These points are known as invariant points, because all the curves pass by these two points. The optimum damper occurs when P and Q reach the same maximum amplitude (Hartog and Pieter, 1985). The optimum value of frequency ratio are given by:

$$f_{ot} = \frac{1}{1 + \mu} \tag{1.5}$$

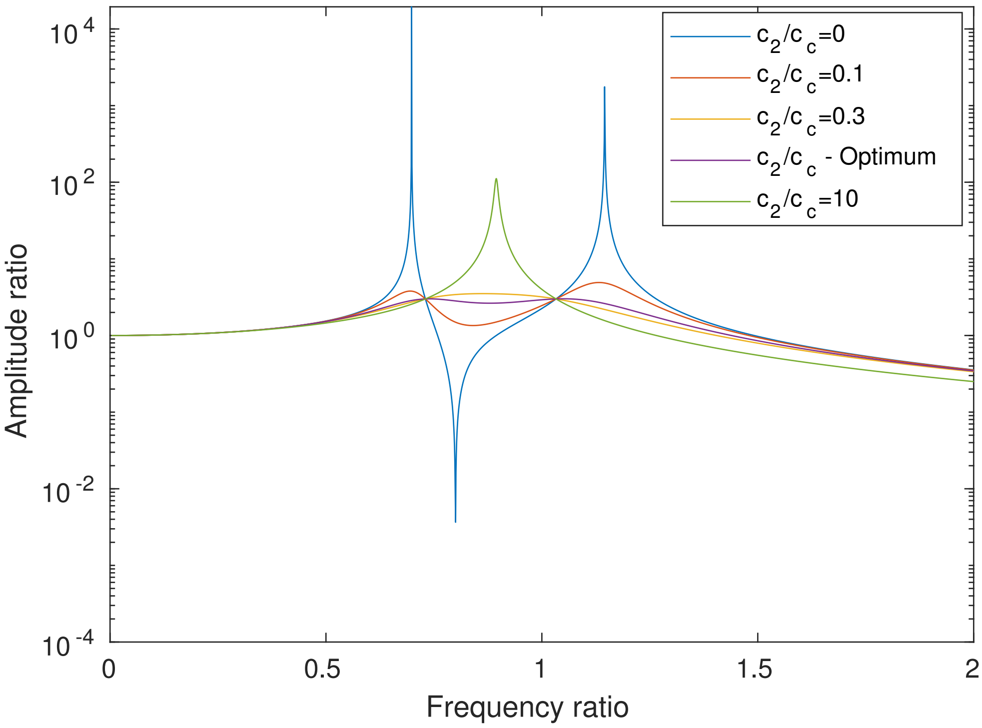

Figure 1.5: Amplitude ratio varying the normalized damping ratio of the absorber, c_2/c_c, as function of the frequency ratio for a primary structure coupled with a dynamic vibration absorber (DVA).

The optimum value for the ratio between damper damping and critical damping are:

$$c_{ot} = \sqrt{\frac{3\mu}{8(1+\mu)^3}} \tag{1.6}$$

Systems characterized by multiple degrees of freedom (MDOF), such as a two-DOF system, possess two normal modes of vibration, consequently resulting in two distinct natural frequencies and two associated generalized coordinates. This increase in complexity makes the design of a single, optimally tuned linear absorber significantly more challenging. While methodologies exist for adapting linear absorbers to MDOF systems Reggio and De Angelis (2015); Ying et al. (2005), these approaches still struggle with the inherent frequency-dependent limitations. Consequently, the inclusion of nonlinear terms becomes decisively more advantageous, particularly when broadband energy absorption is required and when the system's performance must be globally optimized across various excitation conditions. This principle strongly supports the adoption of technologies, such as the PNES, which leverage nonlinearity for enhanced performance.

1.2.1 Consequences of including nonlinear terms

The introduction of cubic or quadratic nonlinear terms fundamentally modifies the dynamic response of a linear mechanical system. Such nonlinear terms influence critical aspects of the system's behaviour, including the amplitude-frequency relationship, system stability, and the characteristics of resonance (Nayfeh and Jebril, 1987). Consequently, the inclusion of nonlinear terms is fundamental for accurately describing systems that inherently possess this characteristic, or for systems where the benefits of altered dynamics, such as enhanced energy absorption or stability augmentation, are desired.

The inclusion of a cubic nonlinear term in the governing equations of a resonator accounts for physical phenomena that linear models fail to capture at high oscillation amplitudes (Nayfeh and Mook, 2008). Depending on the sign of this term, the system exhibits either hardening, where the effective stiffness and resonance frequency increase with amplitude, or softening, characterized by a decrease in stiffness and a leftward tilt of the resonance peak (Kovacic and Brennan, 2011). These behaviours are hallmarks of the Duffing oscillator, a fundamental model used to describe bistability and jump phenomena in micro-mechanical structures (Lifshitz and Cross, 2008). Furthermore, this cubic nonlinearity can be intentionally engineered into a Nonlinear Energy Sink (NES); unlike linear absorbers, a NES lacks a preferential linear resonance frequency, allowing it to capture and dissipate vibrational energy across a broad spectrum through Targeted Energy Transfer (Vakakis et al., 2009), which is critical for enhancing the durability and performance of resonators under fatigue characterization.

The primary objectives for incorporating nonlinear elements into typical aeroelastic systems equipped with energy harvesting capabilities consist of trying to enhance system stability by increasing the critical flutter velocity through efficiently absorb the flutter vibration energy (flutter suppression), and to maximize the electrical output power of the aeroelastic typical section, thereby enabling maximum energy harvesting across a wider frequency range. In a nonlinear context, the flutter velocity is defined as the critical velocity at which the system transitions from a stable equilibrium point to a sustained amplitude of the limit cycle. One of the most extensively investigated nonlinear mechanisms employed to achieve these motivations is nonlinear stiffness (Abdelkefi et al., 2012d). The utilization of such nonlinearity allows the system to overcome the narrow bandwidth limitations inherent to linear absorbers, facilitating robust performance against broadband excitations like those encountered in aeroelastic instability.

Beyond mechanical nonlinearities, other nonlinear elements, such as nonlinear piezoelectric coupling, can also significantly influence the system's dynamic response (Abdelkefi et al., 2012c,b). Consequently, the development of accurate models that define the piezoelectric energy harvester and its operation is of substantial engineering and scientific value. Research by Triplett and Quinn (2009) compared the use of nonlinear stiffness and nonlinear electromechanical coupling against a typical section with linear stiffness and linear electromechanical coupling, providing quantification of flutter velocity, mechanical response, and electrical power output. Their findings demonstrate that the incorporation of nonlinear elements fundamentally alters the system's performance. Specifically, the introduction of nonlinear electromechanical coupling has been shown to increase the system's output power, thereby enabling the extraction of a greater amount of energy.

Specific studies have demonstrated the substantial performance gains achieved by integrating nonlinear elements in both the mechanical and electrical domains. Sousa et al. (2017) utilized the Synchronous Switch Damping in Inductor (SSDI) technique to manage the nonlinear characteristics within the electrical domain, alongside Shape Memory Alloys (SMA) as an alternative to conventional actuators in the mechanical domain. The combined nonlinearity introduced by both the SMA and the SSDI resulted in significantly improved aeroelastic behaviour, achieving stability across a velocity range 25% greater than that of an equivalent linear system. Furthermore, the work of Stanton et al. (2010a,b) highlights the critical importance of incorporating the inherent nonlinearity of piezoelectricity (nonlinear electromechanical coupling) within the energy harvesting circuit models. By accurately reflecting this inherent characteristic, analyses become more precise, ultimately leading to better optimization of the energy output.

A technology that effectively includes nonlinear elements to enhance absorber performance is the Nonlinear Energy Sink (NES). An NES is fundamentally composed of a secondary system (substructure) featuring a nonlinear stiffness element, which is then attached to the main structure. These substructures function as passive, irreversible absorbers of vibrational energy via the mechanism of Targeted Energy Transfer (TET) (Viguié et al., 2009). TET exploits nonlinear modes and internal resonance to achieve the passive and irreversible transfer of vibrational energy from the main system to the NES (Lee et al., 2008b). Specifically, by triggering resonances between the structure's related nonlinear normal modes, energy is irreversibly transferred from the primary structure to the secondary mass of the NES. Research has demonstrated the broad capability of NESs in complex systems. For instance, Zhang et al. (2017b) investigated the wind-induced vibration of a two-dimensional aeroelastic system coupled with two NES units, focusing on the relationship between NESs and TET. The results highlighted that NESs possess the ability to absorb energy from all vibrational modes of the wing, and that TET facilitates more efficient energy transfer both between the system's modes and between the wing and the NESs.

NES, characterized by its essentially nonlinear stiffness, is uniquely capable of absorbing and dissipating energy over a significantly wider range of frequencies compared to its linear counterparts. Furthermore, the work of Jiang et al. (2003) demonstrated that even with weak coupling to the primary linear oscillator, the nonlinear NES is highly effective at absorbing vibration energy from the steady-state response. This superior performance is coupled with additional practical benefits, including low cost and minimal maintenance requirements. These attributes establish the NES as a highly appealing and robust technology for vibration mitigation. Figure 1.6 shows a system with DOF and essentially nonlinear stiffness coupled.

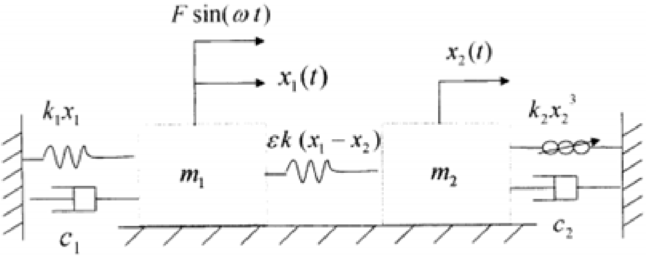

Figure 1.6: System with two degree of freedom and essentially nonlinear stiffness coupled. Source: (Jiang et al., 2003)

NES is commonly employed in aeroelastic systems with the primary goal of reducing vibration amplitude. Bichiou et al. (2016) investigated the use of NES to control flutter and reduce the amplitude of the limit cycle in a two-degree-of-freedom airfoil. Their results indicated that while the increase in flutter velocity was limited, the NES was highly effective at decreasing oscillation amplitude. Importantly, they found that NES effectiveness is dependent on both its location and its mass ratio. Further advancements have explored complex configurations. Lee et al. (2008a) utilized Multiple-Degree-of-Freedom (MDOF) NESs, applied to the aeroelastic system in both series and parallel configurations, comparing them to a single-degree-of-freedom (SDOF) NES. The study revealed that MDOF NESs, when optimally designed, increase the robustness of amplitude suppression. Specifically, the series configuration yielded superior results compared to the parallel arrangement, underscoring the necessity of investigating various configuration strategies for this technology. In pursuit of enhanced efficiency, Boroson et al. (2017) focused on optimizing multiple NESs arranged in parallel to increase the amount of energy absorbed across a wider range of frequencies. Their findings demonstrated that this approach successfully achieved wider excitation ranges coupled with efficient energy dissipation, thereby validating the utility of configuring multiple units to overcome frequency bandwidth limitations.

Lee et al. (2007b) has shown that the NES's performance can range from complete flutter suppression to partial suppression or even be ineffective across certain frequency regimes. In scenarios yielding the most effective suppression, the energy transfer from the wing to the NES is driven by nonlinear modal interactions occurring during resonance. This interaction leads to an exponential decay in the responses of the plunge and pitch modes, as well as the NES itself, ultimately resulting in the elimination of amplitude of the limit cycle. It is generally observed that higher NES mass ratios are required to achieve the complete elimination of amplitudes and to maximize the velocity increase achieved by the suppression mechanism. This highlights the trade-off between mass addition and the desired level of performance enhancement. The aeroelastic typical section incorporating an NES, as investigated by Lee et al. (2007b), is represented in Figure 1.7 and 1.8.

The body of work discussed thus far primarily leverages the mechanical Nonlinear Energy Sink (NES) for energy absorption, aiming to suppress flutter and reduce system oscillation amplitudes. Gendelman (2011) provides a comprehensive overview of the NES's capability for energy mitigation and absorption in both self-excited and externally

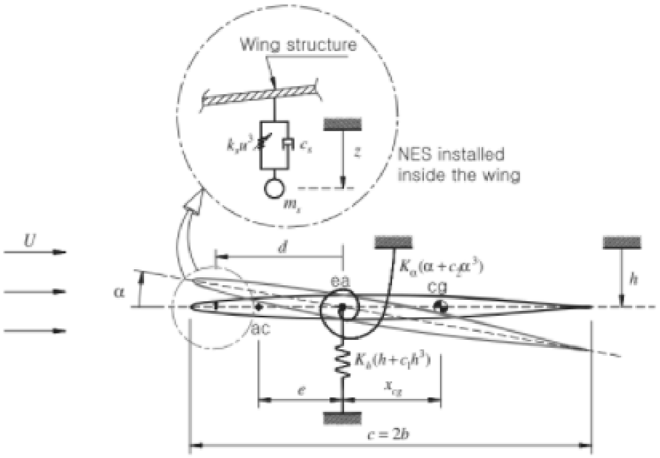

Figure 1.7: Model of aeroelastic typical section model with two degree of freedom with NES coupled. Source: (Lee et al., 2007b)

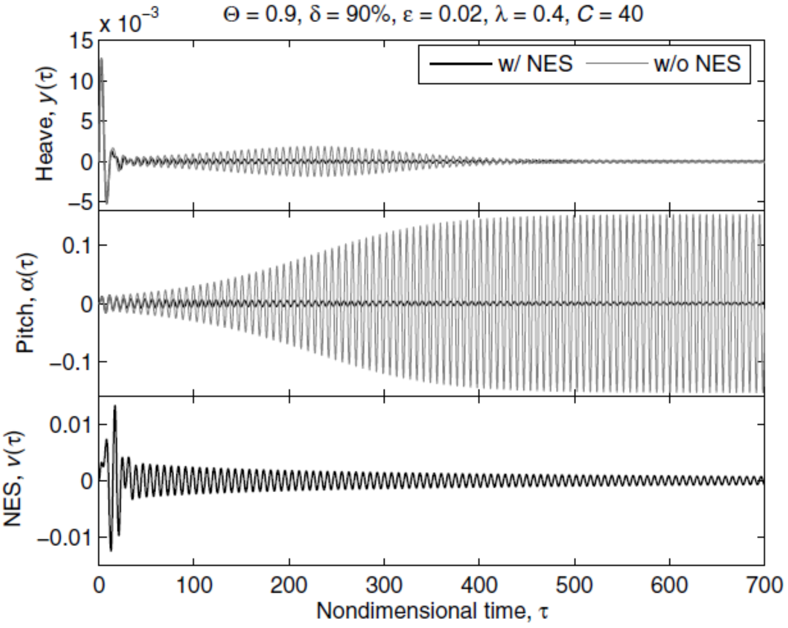

Figure 1.8: Case of best suppression for the system represented in fig. 1.7. Source:(Lee et al., 2007b)

excited systems. Crucially, the NES surpasses the performance of the Tuned Mass Damper (TMD) by achieving vibration suppression and flutter avoidance through a simpler mechanism. Ding and Chen (2020) summarize the developmental trajectory of this technology, highlighting several key design characteristics, such as while systems with larger NES masses exhibit greater effectiveness, research focuses on strategies to reduce the required mass while maintaining performance.

This research project aims to unite two applications of NES, the combination of piezoelectric materials with the NES effectively merges the goals of vibration suppression and energy harvesting, forming Piezoelectric Nonlinear Energy Sink (PNES) (Kang et al., 2024; Zhang et al., 2023). Designing a PNES provides a compelling strategy to re-purpose the absorbed mechanical energy for vibration suppression into usable electrical power. This dual functionality allows for the potential production of electrical power on a large scale from an initial input of mechanical energy. The principle of utilizing piezoelectric elements based on the NES concept has been successfully validated. Silva et al. (2018) experimentally demonstrated significant vibration attenuation using a piezoelectric device based on the NES principle. Their electrical circuit design incorporated a negative capacitance shunt combined with a cubic nonlinear capacitance coupled via amplifiers to a vibrating beam. The proposed model, illustrated in Figure 1.9, was shown to provide robust vibration control. Furthermore, Zhang et al. (2017c) proposed a device explicitly based on the NES principle to achieve simultaneous energy harvesting from the nonlinear energy sink and vibration suppression for the primary structure. This work clearly establishes the feasibility and objectives of the PNES technology. This device is shown in Figure 1.10.

1.3 Uncertainty analysis

As mentioned before, the main advantage of PNES is that energy absorption must occur over a wide range of frequencies. One of the objectives of this work is to compare the

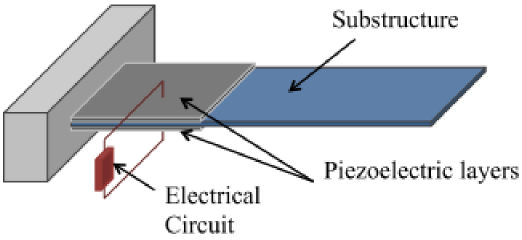

Figure 1.9: Electromechanically coupled beam with shunted piezo layers. Source: (Silva et al., 2018)

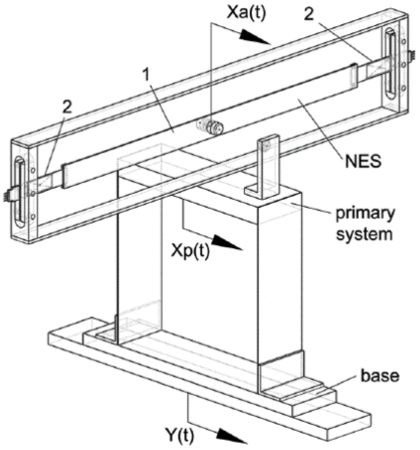

Figure 1.10: Piezoelectric device based on NES, 1-Steel beam and 2-Bimorphic piezoelectrics. Source: (Zhang et al., 2017c)

robustness of PNES and a linear absorber of an aeroelastic system in flutter condition. However, demonstrating this superior robustness is not straightforward. The greater robustness of NES in externally harmonically forced systems is usually demonstrated by a frequency response with the excitation frequency as a control parameter (Barton et al., 2010). This approach is impractical for a system excited by flutter, as flutter is a self-excited phenomenon driven by the interaction of aerodynamic, inertial, and elastic forces. There is no external, controllable forcing function to sweep through a frequency range. This limitation creates a critical gap in the ability to rigorously quantify the performance and robustness of energy harvesters designed for aeroelastic applications.

The performance of any real-world engineering system is inevitably affected by uncertainties stemming from manufacturing tolerances, material property variations, and fluctuating operational environments. In aeroelastic systems, for instance, minor, unavoidable deviations in the stiffness or mass distribution, thermal expansion or aging of a device can lead to significant variations in the critical flutter velocity (Zheng and Wang, 2023). Parametric uncertainty in stiffness and damping of nonlinear aeroelastic systems affects bifurcation points and can lower the onset of flutter (Desai and Sarkar, 2010). Uncertainties also influence the analysis and design of piezoelectric vibration energy harvesters, with significant effects even at relatively low uncertainty levels (Wang et al., 2021; Dash et al., 2022). Quantifying the impact of such uncertainties is therefore an useful step in designing systems that are truly reliable and perform as intended under realistic conditions.

An uncertainty analysis is the most direct and physically relevant method to compare the robustness of PNES and a linear absorber of an aeroelastic system in flutter condition. The system's performance under parametric uncertainties was investigated, evaluating the variability of the harvested power as key properties of the system are varied. The PNES maintains a high level of energy harvesting efficiency across a wide range of uncertain conditions, thereby proving its superior robustness.

1.4 Motivation

Vibration attenuation has long been a critical area of study, given its potential to compromise the integrity of engineering systems. In parallel, energy harvesting has emerged in the last two decades as a promising alternative to non-renewable energy resources. Within this critical context, NES stands out due to their demonstrated ability to suppress flutter and maintain system stability over a wider frequency range compared to traditional linear dynamic vibration absorbers. This broadband capability potentially leads to a significant increase in the amount of energy harvested. The PNES, in particular, offers the unique advantage of simultaneously achieving flutter suppression and converting vibrational energy into electrical power, thus uniting two crucial benefits in a single system.

Recognizing that the main challenge in making energy harvesting viable lies in maximizing the amount of energy captured, and that nonlinear elements represent a promising avenue to achieve this goal, the primary motivation of this work is to compare the advantages and robustness of an aeroelastic typical system with nonlinear terms (specifically, the PNES) to the same system employing a linear absorber under flutter conditions. To realize this comparison, robustness will be determined through the application of an uncertainty analysis, aiming to evaluate the system's sensitivity to parameter variations. Most previous analyses conducted for energy harvesting systems presents greater robustness of NES in externally harmonically forced systems, and it is usually demonstrated by a frequency response with the excitation frequency as a control parameter, which simplifies the problem and does not reflect the complex, non-harmonic nature of the excitation in aeroelastic systems under flutter. This approach is impractical for a system excited by flutter, because there is no external, controllable forcing function to sweep through a frequency range. This limitation creates a critical gap in the ability to rigorously quantify the performance and robustness of energy harvesters designed for aeroelastic applications. Thus, this work aims to fill this gap, offering a more realistic and comprehensive assessment of the PNES's applicability and effectiveness.

1.5 Objectives

The main objective of this work is to define a PNES and analyse its behaviour as an energy harvesting system applied to an aeroelastic typical section in flutter conditions. This main objective is divided into:

- Develop a simplified mathematical model of the aeroelastic typical section to investigate flutter.
- Develop a coupled aerodynamic multibody model of the aeroelastic typical section to verify the simplified mathematical model.
- Analyse the dynamic response of the aeroelastic system with a cubic nonlinear stiffness term.
- Analyse the dynamic response of the aeroelastic system with quadratic electromechanical nonlinear term (PNES).
- Compare the robustness of the system with nonlinear terms to the system with linear absorber using uncertainty analysis.

Chapter 2

Methodology

In this section the methodology of the project is presented. The design of a piezoelectric transducer is described and compared to a classic DVA (dynamic vibration absorber). The response of the aeroelastic typical section is studied through four methods: eigenvalues classical method using a low order model with Dowell aerodynamic loads (LOM-Dowell model), commercial CFD (computational fluid dynamics) software solver STAR-CCM+ using a coupled aerodynamics multibody model to simulate flutter (multibody-CFD model), multiple scales method (MMS) and 4th order Runge-Kutta simulation (RK). All the methods are presented in this chapter. To encompass all variations of the studied system, four cases are proposed in this work.

Figure 2.1 illustrates the methodology and theirs applications.

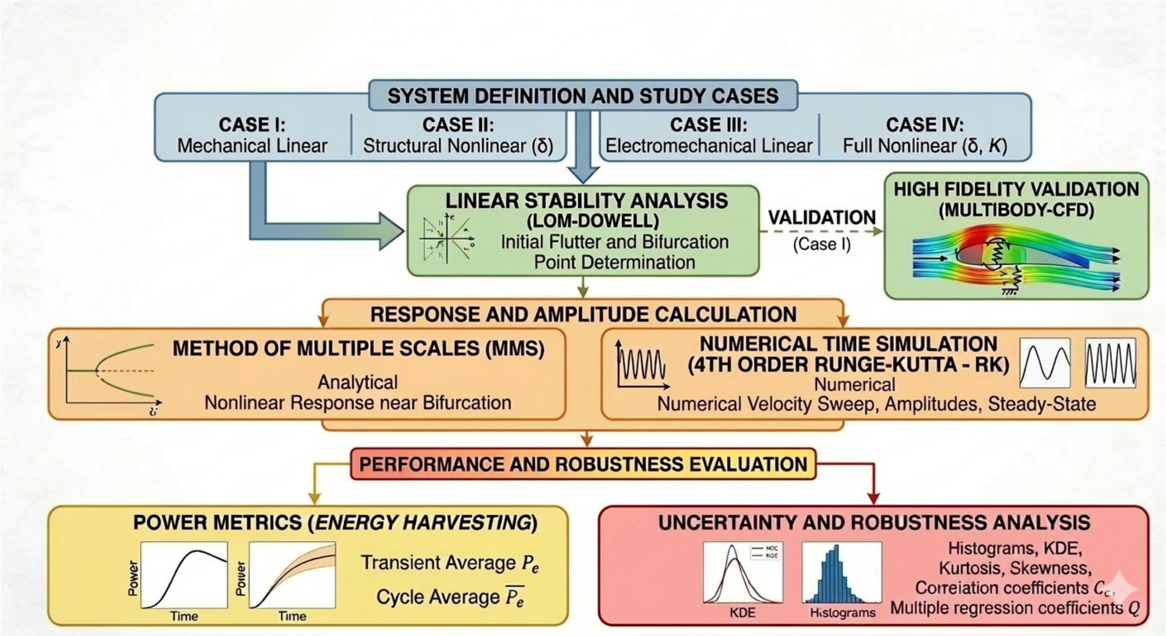

Figure 2.1: Flowchart of methodology.

2.1 Comparison between a mechanical damper and a piezoelectric transducer

As described in chapter 1, piezoelectric transducer is equivalent to a mechanical damper, with the difference of being able to produce power using energy harvesting technology. Therefore, comparing a piezoelectric transducer to a mechanical damper is interesting to better understand the functioning of the electrical absorber, since the mechanical absorber has already been widely known and studied.

The one DOF system with mechanical damper can be represented by the following equation:

$$\begin{aligned} m_1\ddot{x}_1 + c_1\dot{x}_1 + k_1x_1 + k_2(x_1 - x_2) + c_2(\dot{x}_1 - \dot{x}_2) = 0 \\ m_2\ddot{x}_2 + k_2(x_2 - x_1) + c_2(\dot{x}_2 - \dot{x}_1) = 0 \end{aligned} \tag{2.1}$$

in which m_1 is the mass of the main system, c_1 is the damping of the main system, k_1

is the stiffness of the main system, m_2 is the mass of the damper, c_2 is the damping of the damper and k_2 is the stiffness of the damper.

The one DOF system with electrical damper can be represented by the following equation:

$$\begin{aligned} m_1\ddot{x_1} + c_1\dot{x_1} + k_1 x_1 - \frac{\theta}{C_p} q = 0 \\ L\ddot{q} + R\dot{q} + \frac{q}{C_p} - \frac{\theta}{C_p} x_1 = 0 \end{aligned} \tag{2.2}$$

in which m_1 is the mass of the main system, c_1 is the damping of the main system, k_1 is the stiffness of the main system, L is the inductance of the electric damper, R is the electric resistance of the electric damper, C_p is the capacitance of the electric damper and θ is the electromechanical coupling of the electric damper.

For the comparison between the mechanical and electrical models, the equations 2.1 and 2.2 are separated into a stiffness, damping and mass matrix. The stiffness matrices for mechanical and electric, respectively, are:

$$K_m = \begin{bmatrix} k_1 + k_2 & -k_2 \\ -k_2 & k_2 \end{bmatrix} \tag{2.3}$$

$$K_e = \begin{bmatrix} k_1 & -\theta/C_p \\ -\theta/C_p & 1/C_p \end{bmatrix} \tag{2.4}$$

Through the matrices K_m and K_e, it is possible to see the equivalence of the electrical and mechanical dampers terms: θ is directly proportional to k_2, C_p is inversely proportional to k_2. If we increase θ, we are increasing the stiffness of the damper, which increases the equivalent stiffness of the system, and consequently a decrease in the amplitude of the system. So, it increases the flutter velocity. It also increases the passage of energy from mechanical power to electrical power, as it increases the system's energy harvest. It can be seen that C_p has the opposite behavior of θ.

The damping matrices for mechanical and electric, respectively, are:

$$C_m = \begin{bmatrix} c_1 + c_2 & -c_2 \\ -c_2 & c_2 \end{bmatrix} \tag{2.5}$$

$$C_e = \begin{bmatrix} c_1 & 0 \\ 0 & R \end{bmatrix} \tag{2.6}$$

As R is equivalent to mechanical damper damping c_2,increase value of R decreases the amplitude of the system until an optimum value. Increase possibilities a better energy harvesting, until the optimum point.

The mass matrices for mechanical and electric, respectively, are:

$$M_m = \begin{bmatrix} m_1 & 0 \\ 0 & m_2 \end{bmatrix} \tag{2.7}$$

$$M_e = \begin{bmatrix} m_1 & 0 \\ 0 & L \end{bmatrix} \tag{2.8}$$

L is equivalent to mechanical damper mass m_2, it is responsible, with stiffness, to form natural frequency of the system. So, increase damper mass decreases damper frequency.

2.2 Analysis of system response

The aeroelastic system is analysed through four methods: eigenvalues classical method using a low order model with Dowell aerodynamic loads (LOM-Dowell model), commercial CFD (computational fluid dynamics) software solver STAR-CCM+ using a coupled aerodynamics multibody model to simulate flutter (multibody-CFD model), multiple scales method (MMS) and 4^{th} order Runge-Kutta simulation (RK).

Firstly, the stability of the LOM-Dowell model is analysed using eigenvalues. This particular method can only be used for purely linear systems. For eigenvalues, whose real part is negative, the system is stable. When the system has a positive real part of one or more eigenvalues, the system is unstable. Flutter occurs at the bifurcation point of the system when the solution changes from an equilibrium point to a limit cycle oscillation (LCO).

The inclusion of nonlinear terms in the aeroelastic typical section makes the use of different methodologies necessary to analyse the system response. Another option for investigating the aeroelastic system is commercial CFD (computational fluid dynamics) software solver STAR-CCM+ using a coupled aerodynamics multibody model to simulate flutter (multibody-CFD model). This method is supposed to yield a better representation of the aerodynamic system under consideration, so it can be an interesting tool to check the eigenvalues method. Furthermore, it accepts nonlinear elements to be added to the system.

Multiple scales method (MMS) is an analytical method for calculating the response of the system near the center or focus Nayfeh and Balachandran (2008), the response is represented as a function of multiple independent variables or scales, rather than a single variable. With this method, it is only necessary to find the eigenvectors associated with the eigenvalues in the bifurcation point. One of the advantages of this method is that it allows to solve the equations in the presence of damping and nonlinearity, unlike other methods such as the Lindstedt-Poincaré method. As the work used numerical solutions, it is interesting to have an analytical solution as well.

The aeroelastic system's movement is modeled using a 4th order Runge-Kutta simulation (RK) coupled with a sequential parameter search. To identify the flutter velocity, a velocity sweep is performed: the system response is simulated across an increasing range of flow speeds. For each step, the algorithm monitors the response peaks to detect convergence. Through this optimization and scanning process, it is possible to determine the flutter velocity and the resulting steady-state amplitudes of the movement. These results are then used to calculate the average harvested power per cycle. This power-harvesting potential must be mapped for each unique combination of structural and electrical parameters to identify the optimal configuration for energy harvesting.

2.2.1 Settings for CFD analysis

In this subsection, the CFD method is explained in more detail. The flutter velocity is calculated through a sequential search using coupled aerodynamic multibody model and Unsteady Reynolds Averaged Navier-Stokes (URANS) simulations to obtain unsteady aerodynamic. The commercial CFD solver STAR-CCM+ is used to simulate flutter in aeroelastic typical section and to determine flutter velocity. The geometry chosen for the simulation was NACA 0012, due a large previous reference. Table 2.1 shows initial conditions for the aeroelastic typical section and table 2.2 shows initial conditions of the fluid.

Table 2.1: Aeroelastic typical section

Geometry	NACA 0012
Chord length	0.250 m
Elastic axis	25% of chord length

Table 2.2: Fluid

Type	21 graus Celsius
Pressure	101325 Pa

To model the fluid flow it was used URANS are carried out using an implicit time marching and a k-ω SST turbulence model as can be seen in table 2.3. The initial conditions for the domain are shown in table 2.4

Table 2.3: Models

All y + Wall treatment
Gas
Gravity
Ideal Gas
Implicit unsteady
K-Omega Turbulence
Overset conservation
Reynolds-Averaged Navier-Stokes
Segregated Flow
Segregated Fluid Temperature
Solution Interpolation
SST (Menter) K-Omega
Turbulence
Two Dimensional
Wall Distance

Table 2.4: Domain

Pressure	0 Pa
Static Temperature	294.15 K
Turbulence intensity	0.05
Velocity	8.3-8.5 m/s

Computational Domain and Meshing

To realize the simulation, an overset mesh for the airfoil motion and a background mesh for the domain were used. For the overset mesh, which is moving with respect to the body, the quadrilateral mesher is used together with the prism layer mesher, while for background mesher, remaining unaltered throughout the simulation, only quadrilateral mesher is used. The base size for the background mesh was 0.125 m, and for the overset mesh was 0.05 m. A wake refinement is realized after the airfoil wing. The final mesh settings after refinements are shown in tables 2.5, 2.6, 2.7 and 2.8. Figure 2.2 shows the mesh used as it was described.

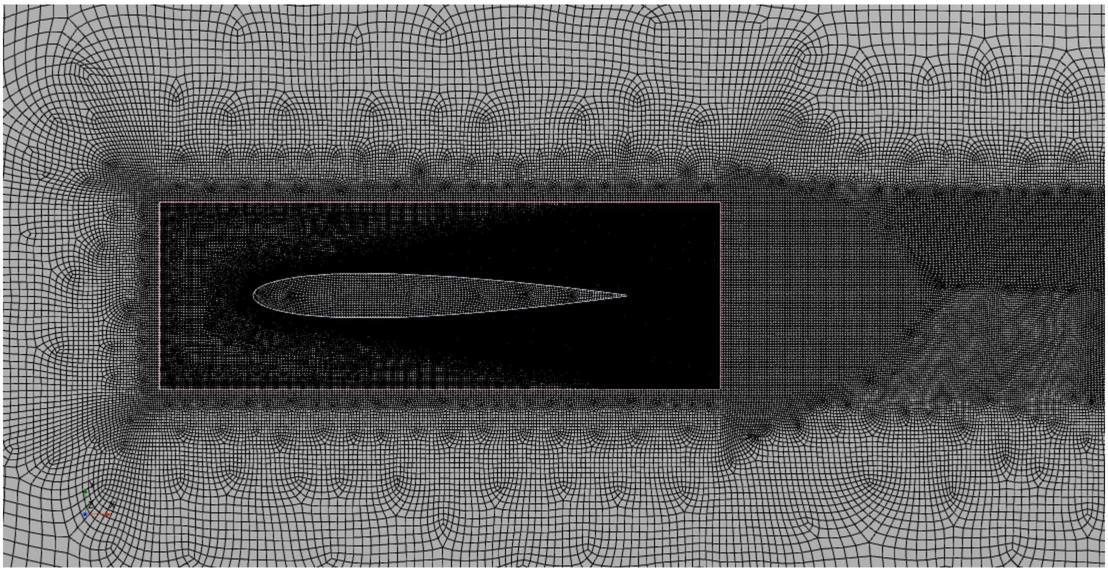

Figure 2.2: Computational mesh.

Table 2.5: Default Controls

Base size	0.125 m
Target surface size	120% of base
Minimum surface size	1% of base
Surface growth rate	Slow
Wake refinement	7% of base

Table 2.6: Wake refinement

Isotropic size	7% of base

Table 2.7: Default Controls

Base size	0.05 m
Target surface size	20% of base
Minimum surface size	1% of base
Surface growth rate	Slow
Number of Prism Layers	15
Prism Layer Stretching	1.5
Prism Layer Total thickness	0.00625 m

Table 2.8: Wake refinement

Spread Angle	0.2 radian
Isotropic size	5% of base

Boundary Conditions

In the overset region, the boundary types applied were Wall, and Overset mesh for the boundary between the overset and background region. In the background region, Symmetry conditions were used for the upper and lower boundaries. For the inlet, it was used Velocity Inlet, with velocity equal 8.8 m/s, and for outlet boundaries it was used Pressure Outlet with pressure equal 0 Pa. For the inlet and outlet boundaries, the boundary conditions can be seen in tables 2.9 and 2.10. Figure 2.3 shows a sketch of the set up.

Table 2.9: Inlet

Boundary type	Velocity inlet
Static temperature	294.5 K
Turbulence intensity	0.05
Turbulence Viscosity radio	10
Velocity	8–10 m/s

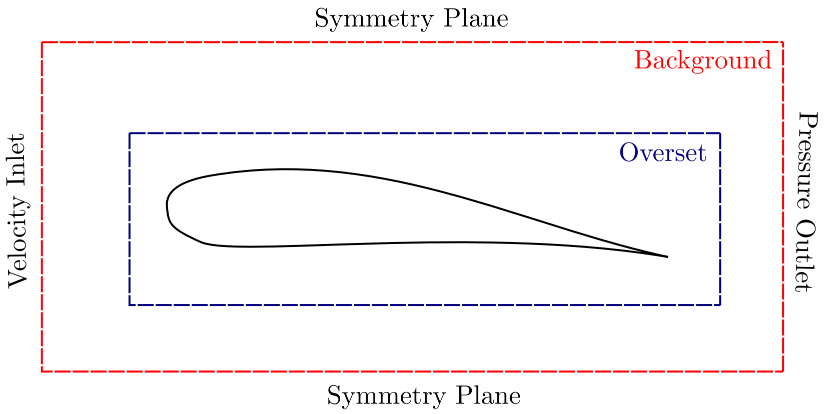

Figure 2.3: Background region and Overset region with boundary conditions.

Table 2.10: Outlet

Boundary type	Pressure outlet
Static temperature	294.5 K
Turbulence intensity	0.05
Turbulence Viscosity radio	10
Pressure	0 Pa

Dynamic Fluid Body Interaction (DFBI)

To include desired constrains and couplings (stiffness and damping)in the system, the tool, Dynamic Fluid Body Interaction (DFBI) motion, allows free motion at determined degrees of freedom, and definition constrains and couplings. Also the cubic nonlinear stiffness can be included and studied. The settings for center of gravity and moment of inertia were the same defined as nominal structure parameters. For the aeroelastic typical section there is two mechanical degrees of freedom: pitch (Z motion) and plunge (Y motion). The weighted average of the aeroelastic typical section and its fixation mass is calculated to determine the center of mass. The airfoil mass m is equal 0.804 Kg and its center is fixed in 0.125 m. The fixation mass m_e is equal 1.06 kg and its center is fixed in elastic axis in 25% of the chord. Finally the weighted average will be 0.07975 m, which do not correspond to the aerodynamic center. The moment of inertia, stiffness and damping are all nominal parameters of the system. The translation spring-damper has a fixed value, and it is fixed in the elastic axis, the rotational spring depends of the rotational DOF, pitch, and is fixed in the elastic axis, as well, and rotational damping is included as a damping moment. Table 2.11 shows the DFBI settings.

Table 2.11: DFBI settings

Free motion	
X motion	No
Y motion	Yes
Z motion	Yes
Initial Values	
Angular Velocity	0
Center of Mass	[0.07975, 0, 0] m, m, m
Moment of Inertia	0.0028 kgm^2
Velocity	[0, 0, 0]
External Forces and Moments	
Damping Moment	0.0199 Nms/rad
Spring-Damper	
Position 1	[-0.01725, 0, 0] m, m, m
Position 2	[0.0625, -0.001, 0] m, m, m
Relaxation length	0 m
Coordinate system 1	Laboratory -> Body 2D 1-CSys
Coordinate system 2	Laboratory
Elastic Coefficient	2100 N/m
Damping Coeffient	1.877 Ns/m
User-Defined	
Position 1	[-0.01725, 0, 0] m, m, m
Position 2	[0.0625, -0.001, 0] m, m, m
Coordinate system 1	Laboratory -> Body 2D 1-CSys
Coordinate system 2	Laboratory
Compute Moments	Yes
Moment Profile	[0, 0, -2.65(α)] Kgm^2

Note: Position 1 has the center of mass as reference, so $0.0625 - 0.07975 = -0.01725$ m. Position 2 has the center of the system as reference, which is in the beginning of the airfoil. The relaxation length are determined in Position 2, as well.

Nonlinear elements

To include cubic nonlinear stiffness, a new spring-damper setting in the DFBI is included with elastic coefficient in function of the cubic nonliear stiffness coefficient (δ), as we can see in table 2.12.

Table 2.12: DFBI settings

Spring-Damper 2	
Position 1	[-0.01725, 0, 0] m, m, m
Position 2	[0.0625, -0.001, 0] m, m, m
Relaxation length	0 m
Coordinate system 1	Laboratory -> Body 2D 1-CSys
Coordinate system 2	Laboratory
Elastic Coefficient	$\delta \times 10^7 h^2$ N/m
Damping Coeffient	0 Ns/m

2.2.2 Multiple scales method

In this subsection, the MMS is demonstrated. Following the method of multiple scales as described in Ghommem et al. (2010), system equation must be put in the form:

$$\dot{Y} = F(Y, U) \tag{2.9}$$

To present Hopf bifurcation when $U = U^*$, a small dimensionless parameter ϵ is introduced. Wind velocity is expanded as follows: $U = U^* + \epsilon^2 \sigma_U U^*$. A third-order solution is sought in the form:

$$Y(t, \sigma_U) = \epsilon Y_1(T_0, T_2), \epsilon^2 Y_2(T_0, T_2), \epsilon^3 Y_3(T_0, T_2) \tag{2.10}$$

The derivative time is written as follows:

$$\frac{d}{dt} = D_0 + \epsilon^2 D_2 + \epsilon^3 D_2 \tag{2.11}$$

Replacing eq.(2.10) and eq.(2.11) in eq.(2.9), and separating equations according to the powers of ϵ results in:

$$D_0 Y_1 - A(U^*) Y_1 = 0 \tag{2.12}$$

$$D_0 Y_2 - A(U^*) Y_2 = Q(Y_1, Y_1) \tag{2.13}$$

$$D_0 Y_3 - A(U^*) Y_3 = -D_2 Y_1 + \sigma_U B Y_1 + 2Q(Y_1, Y_2) + C_c(Y_1, Y_1, Y_1) \tag{2.14}$$

in which Q is the quadratic nonlinear vector C_c is the cubic nonlinear vector, and B is the matrix that contains the coefficients of σ_U.

The eigenvectors of matrix B are also required in the method. The right eigenvector is represented by p, and the left eigenvector is represented by q_q which is normalized as:

$$q = \frac{q_q}{|q_q^T p|} \tag{2.15}$$

System response for the multiple scale method is given by:

$$a = \sqrt{\frac{-4\beta}{\Lambda_a}} \tag{2.16}$$

in which the parameters Λ_a and β are given by:

$$\Lambda_a = 4q^T Q(p, \zeta_0) + 2q^T Q(\overline{p}, \zeta_2) + 3q^T C_c(p, p, \overline{p}) \tag{2.17}$$

$$\beta = q_q^T \sigma_U B p \tag{2.18}$$

The values of ζ_0 e ζ_2 can be calculated through the equations:

$$\zeta_0 = \frac{-Q(p, \overline{p})}{A(U^*)} \tag{2.19}$$
$$\zeta_2 = \frac{Q(p, p)}{2i\omega I - A(U^*)}$$

2.2.3 Uncertainty analysis

The robustness of the aeroelastic system is assessed through a probabilistic approach using the Monte Carlo Simulation (MCS) method (Papadopoulos and Yeung, 2001; Rubinstein and Kroese, 2016). The primary statistical metrics and visualizations used to compare the robustness of the system are Output Coefficient of Variation (λ_o), Kernel Density Estimate (KDE) Plots, Histograms, Kurtosis, Skewness, Correlation Coefficients (C_c) and Multiple Regression Coefficients (Q).

For each simulation, a set of 100 samples was generated. Key mechanical, electrical, and electromechanical input parameters were treated as uncertain variables. Their probabilistic distributions were defined based on deterministic nominal values (μ_n), which were informed by similar models and experimental results in the literature.

Assuming independent normal distributions for each parameter, with mean equal to the nominal value, the standard deviation (σ) for the sampling was calculated using a prescribed coefficient of variation for the input, which is given by:

$$\lambda_i = \frac{\sigma}{\mu_n} \tag{2.20}$$

To investigate the system's sensitivity to varying levels of uncertainty, two scenarios were analysed with λ_i values of 5% and 15%. The effect of these input uncertainties on the system's performance was quantified by calculating the coefficient of variation of the output (λ_o), which in this case is the electrical power. This metric serves as the primary basis for comparing the variability and the robustness of the system with or without nonlinear terms.

2.2.4 Electrical power metrics

To evaluate the energy harvesting performance under both transient and steady-state conditions, two distinct average power metrics were computed from the instantaneous electric power ($P_{ei} = R\dot{q}^2$) from the time-domain simulations:

- Transient Average Power (P_e): calculated by integrating the instantaneous power over a specified period of the transient regime (from 0 s to 7 s) using the trapezoidal method and dividing by that period.

- Steady-State Average Power per Cycle ($\overline{P_e}$): calculated by integrating the instantaneous power over the last cycle within the steady-state regime and dividing the result by the period of that cycle.

2.3 Proposed cases

As mentioned in the beginning of this section, there are four cases that are evaluated in this work:

- Case I: Aeroelastic typical section, without piezoelectric coupling, with two mechanical DOFs, purely linear.
- Case II: Aeroelastic typical section, without piezoelectric coupling, with two mechanical DOFs, with cubic nonlinear stiffness ($\delta = 2 \times 10^7$ N/m^3).
- Case III: Aeroelastic typical section, with piezoelectric coupling, with two mechanical and one electrical DOFs, purely linear.
- Case IV: Aeroelastic typical section, with piezoelectric coupling, with two mechanical and one electrical DOFs, with cubic nonlinear stiffness ($\delta = 2 \times 10^7$ N/m^3) and with quadratic nonlinear electromechanical coupling ($K = 10$).

Case I is dedicated to the validation of the LOM-Dowell model through multibody-CFD model, ensuring its fidelity for systematic application across all subsequent analyses. Case II focused on characterizing the influence of the structural parameter δ on the purely mechanical system response. Robustness assessment is conducted through uncertainty analysis, comparing the Case III to the Case IV. Case IV also served to evaluate the sensitivity of the energy harvesting performance to variations in both the nonlinear terms and the electrical parameters.

Chapter 3

Mathematical model

In this section, the piezo-structural model and the dynamical equations of aeroelastic typical section are described. Also, three mathematical models for aerodynamic loads are presented. In chapter 4 aerodynamic models are compared.

3.1 Piezo-structural model

Figure 3.1 shows the piezo-structural model, it is used a low order model (LOM) of an aeroelastic typical section characterised by three degrees of freedom: plunge (h), pitch (α), and the electrical charge (q) across the piezoelectric transducer. The piezoelectric coupling is associated to plunge. O is the elastic axis, C is the centroid, c is chord length and b is the semi-chord length.

The dynamical equations, based on Marqui Jr and Erturk (2013), of the system presented in Fig. 3.1, applying nonlinear stiffness of the cubic type associated to plunge

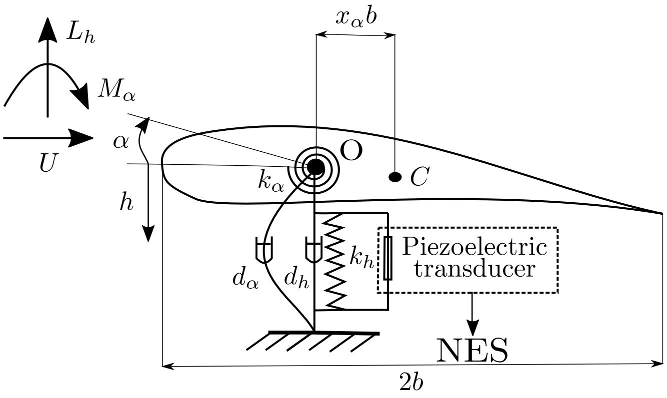

Figure 3.1: Aeroelastic section.

movement and quadratic nonlinear electromechanical coupling are given by:

$$\begin{aligned}(m+m_e)\ddot{h}+mbx_\alpha\ddot{\alpha}+d_h\dot{h}+k_hh+\delta h^3-\frac{\theta}{C_p}(K|h|+1)q&=-L_h \\ mbx_\alpha\ddot{h}+I_\alpha\ddot{\alpha}+d_\alpha\dot{\alpha}+k_\alpha\alpha&=M_\alpha \\ L\ddot{q}+R\dot{q}+\frac{q}{C_p}-\frac{\theta}{C_p}(K|h|+1)h&=0\end{aligned} \tag{3.1}$$

in which m is the airfoil mass, m_e is the fixture mass, bx_α is the distance between elastic axis and centroid, h is plunge DOF, α is pitch DOF, d_h and d_α are damping coefficients for plunge and pitch, respectively, k_h and k_α are stiffness coefficients for plunge and pitch, respectively, I_α is the moment of inertia, ω_h and ω_α are uncoupled natural frequency for plunge and pitch, respectively, q is electrical charge, R is electrical resistance, C_p is equivalent piezoelectric capacitance, θ is electromechanical coupling, L is electrical inductance, δ is the cubic nonlinear stiffness coefficient, K is the quadratic nonlinear electromechanical coupling coefficient, L_h is aerodynamic lift, M_α is aerodynamic moment and U is the airflow velocity, and . denotes differentiation by time.

3.2 Aerodynamic model

To work with aeroelastic systems, it is important to define the aerodynamic loads. The first aerodynamic loads are presented in matrix form, by Edwards (1979), for unstable model and incompressible flow. The aerodynamic matrix equations of lift (L_h) and moment (M_α) for this model are:

$$\begin{bmatrix} I & 0 & 0 & 0 \\ 0 & \tilde{M} & 0 & 0 \\ 0 & 0 & I & 0 \\ 0 & 0 & 0 & \eta \end{bmatrix} \begin{bmatrix} x' \\ x'' \\ x'_a \\ \overline{v}' \end{bmatrix} = \begin{bmatrix} 0 & I & 0 & 0 \\ -\tilde{K} & -\tilde{B} & D & \theta_1 \\ E_1 & E_2 & F & 0 \\ 0 & -\theta_2 & 0 & -\frac{1}{\lambda_l} \end{bmatrix} \begin{bmatrix} x \\ x' \\ x_a \\ \overline{v} \end{bmatrix} \tag{3.2}$$

in which $\theta_1 = [0 \quad \kappa]^t$, $\theta_2 = [0 \quad \kappa]$, $x = [a \quad \overline{h}]^t$, $x_a = [x_1 \quad x_2]^t$, I is identity matrix 2x2, $\tilde{M}$, $\tilde{B}$, $\tilde{K}$ are calculated through structural matrix of mass, damping and stiffness, respectively. $\tilde{M}$, $\tilde{B}$, $\tilde{K}$ and aerodynamic matrix D, E_1, E_2, F can be found in Edwards (1979).

Dimitriadis (2017) presents another aerodynamic model, for a quasi-steady aerodynamics (without vortices effect) and incompressible flow. The equations are reproduced below:

$$\begin{aligned} L_h &= \rho\pi b^2\left(\ddot{\overline{h}} - \left(e - \frac{c}{2}\right)\ddot{\alpha}\right) + \rho\pi b^2\overline{U}\dot{\alpha} + \rho\overline{U}^2 c\pi\left(\alpha + \frac{\dot{\overline{h}}}{\overline{U}} + \left(\frac{3}{4}c - e\right)\frac{\dot{\alpha}}{\overline{U}}\right) \\ M_\alpha &= \rho\pi b^2\left(e - \frac{c}{2}\right)\left(\ddot{\overline{h}} - \left(e - \frac{c}{2}\right)\ddot{\alpha}\right) - \frac{\rho\pi b^4}{8}\ddot{\alpha} - \left(\frac{3}{4}c - e\right)\rho\pi b^2\overline{U}\dot{\alpha} \\ &\quad + \rho\overline{U}^2 e_f c^2\pi\left(\alpha + \frac{\dot{\overline{h}}}{\overline{U}} + \left(\frac{3}{4}c - e\right)\frac{\dot{\alpha}}{\overline{U}}\right) - \frac{1}{16}\rho\overline{U}c^3\pi\dot{\alpha} \end{aligned} \tag{3.3}$$

in which, $\overline{h}$ is plunge DOF,α is pitch DOF, c is chord length, L_h is aerodynamic length, M_α is aerodynamic moment, $\overline{U}$ is the airflow velocity, ρ is density, b is semichord length, e is the distance from the beginning of the airfoil and aerodynamic center, and $e_f = e/c - 1/4$.

Dowell et al. (1989) also presents a mathematical model for aerodynamic loads, for a quasi-steady system and incompressible flow, it includes the contribution of the angle of attack. The equations are reproduced below:

$$\begin{aligned} L_h &= qS\frac{\partial C_L}{\partial \alpha}\left[\alpha + \frac{\dot{h}}{U}\right] \\ M_\alpha &= qSe\frac{\partial C_L}{\partial \alpha}\left[\alpha + \frac{\dot{h}}{U}\right] \end{aligned} \tag{3.4}$$

in which, h is plunge DOF, α is pitch DOF C_L is the lift coefficient, ρ is airflow density, U is airflow velocity, e is the distance between aerodynamic center and elastic axis. For a flat plate with incompressible flow, we can consider $\partial C_L/\partial\alpha = 2\pi$, $C_{L0} = C_{MAC} = 0$, $q = \rho U^2/2$ and $S = 2b$.

It should be noted that the equations of aerodynamic loads are dependent on U; as the system input, U is directly embedded within the dynamic equations.

3.3 Nominal parameters

The values of nominal parameters used here are: $m = 0.804$ kg, $m_e = 1.060$ kg, $b = 0.125$ m, $x_\alpha = 0.2064$, $d_h = 1.8770$ Ns/m, $d_\alpha = 0.0199$ Nms/rad $k_h = 2100$ N/m, $k_\alpha = 2.65$ Nm/rad, $\rho = 1.07$kg/m^3, $\theta = 0.00155$ N/V, $C_{res} = 0.00005$ F, $I_\alpha = 0.0028$ kg m^2, $L = 22$ H, $R = 330000\ \Omega$, $U = 5.56$ m/s, $\delta = 0$ and $K = 0$. The initial conditions used are: $h = 0.003$ m, $\alpha = 0$, $h' = 0$, $\alpha' = 0$ and $q = 0$.

Chapter 4

Aerodynamic model validation

In this chapter, aerodynamic loads proposed by Edwards, Dimitriadis and Dowell are compared to each other. The flutter velocity is determined for Case I with two analysis. First, through eigenvalues for LOM-Dowell model, and second, using a sequential search for multibody-CFD model. Comparison between both linear analysis are realized through calculation of the moment and lift as function of angle of attack. Also, cubic nonlinear stiffness are included and the influence of this nonlinear element in the system response is evaluated for Case II.

The comparison between Edwards and Dimitriadis aerodynamic models was realized using the system proposed by Amaral et al. (2023). This work contributed with the Dowell model. Dowell model is formed by simplified equations, which can facilitate the use of analytical methods. For Ding and Chen (2020), work that shows a completed review about NES and its trends, the most references for aeroelastic typical sections used Dowell model, which corroborates the study of the model in this work (Lee et al., 2007a,b, 2008a; Zhang et al., 2019, 2017b; Tian et al., 2019).

Figure 4.1 shows variation of flutter velocity (U^*) as function of dimensionless electromechanical coupling (κ), for the three aerodynamic models previous presented. The response was calculated, analytically. We can noticed that Dowell model presents a smaller value of flutter velocity, but the same trend of the other aerodynamic methods. Given its simplified equation structure and its validated ability to predict the same qualitative trend as more complex models, a finding that is further corroborated by its broad adoption in the literature on nonlinear aeroelastic analysis, the Dowell model was selected for the subsequent investigations presented in this work.

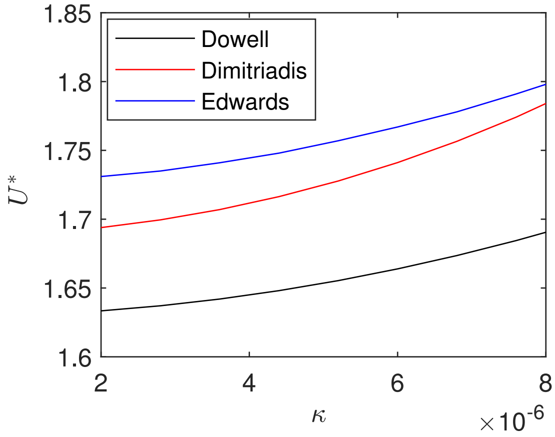

Figure 4.1: Flutter velocity as function of dimensionless eletromechanical coupling, using Dowell, Dimitriadis and Edwards models.

4.1 Flutter velocity evaluation

The stability of the equivalent LOM-Dowell model was determined by analysing the system's eigenvalues as a function of wind velocity. As shown in Fig. 4.2, the real and imaginary parts of the eigenvalues indicate a critical flutter velocity of $U^* = 5.56$ m/s. For the multibody-CFD model, the flutter velocity was determined using a sequential search method, yielding a higher critical velocity of $U^* = 8.8$ m/s.

To continue investigating the system's stability of LOM-Dowell model, the time response is determined in Fig. 4.3 using $U^* = 5.56$ m/s. We can notice that for U^*, all the peaks reach the same amplitude.

Now, U^* is determined using a sequential search for multibody-CFD model. Figure 4.4 shows the time response for flutter velocity $U^* = 8.8$ m/s. Comparing the multibody model against the simplified model, the multibody model presents a bigger U^*, and

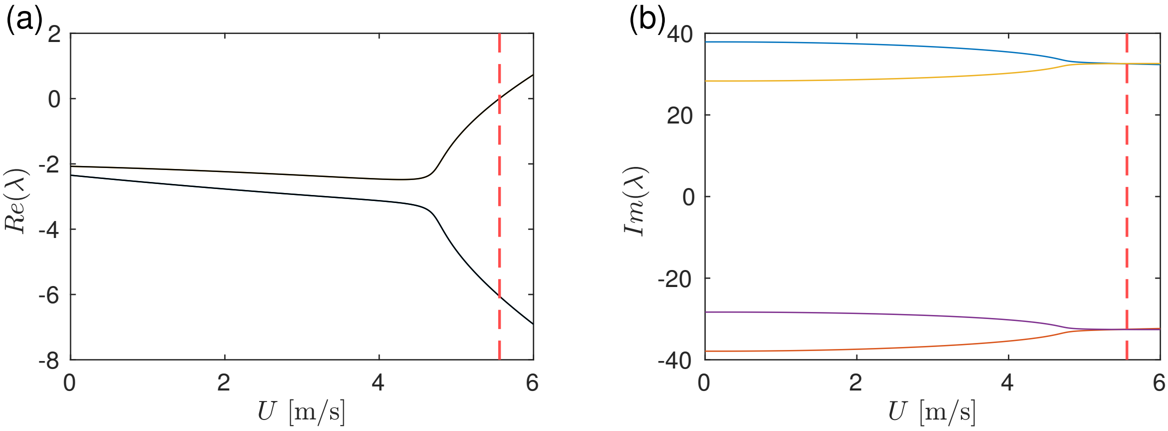

Figure 4.2: Real (a) and imaginary (b) part of eigenvalues of the equivalent LOM-Dowell model as function of wind velocity. Flutter velocity is indicated by the dashed line.

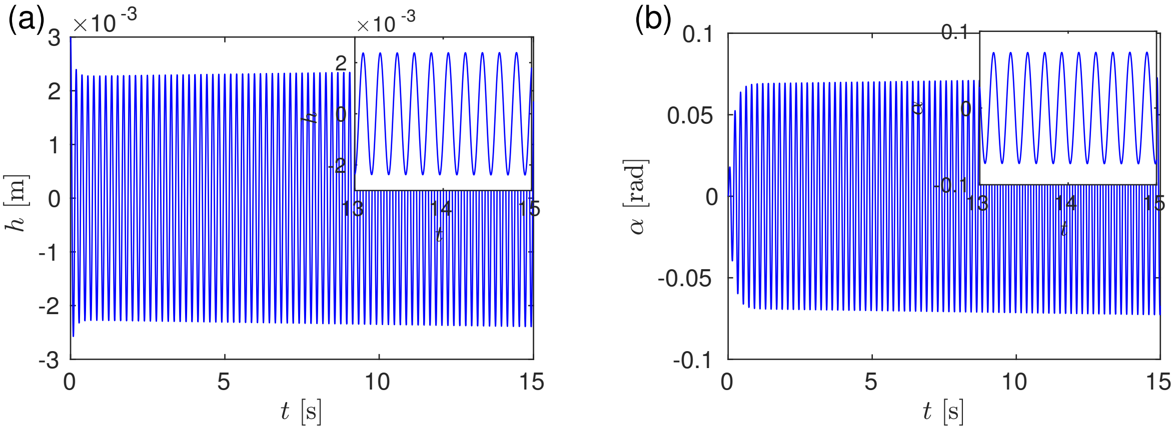

Figure 4.3: a) Plunge movement b) Pitch movement for $U^* = 5.56$ m/s, using LOM-Dowell model.

a larger amplitude. A first comparison between the simplified model and the coupled aerodynamic multibody model is given by resonance frequency. For the simplified model, the resonance frequency equals 5.20 Hz, with an amplitude equal to 2.36×10^{-3} m for plunge, and equal to 7.16×10^{-2} rad for pitch. For the multibody model, the resonance frequency equals 5.80 Hz with an amplitude equal to 7.31×10^{-3} m for plunge, and equal to 12.5×10^{-2} rad for pitch. We can consider a good agreement between both models and the same trend.

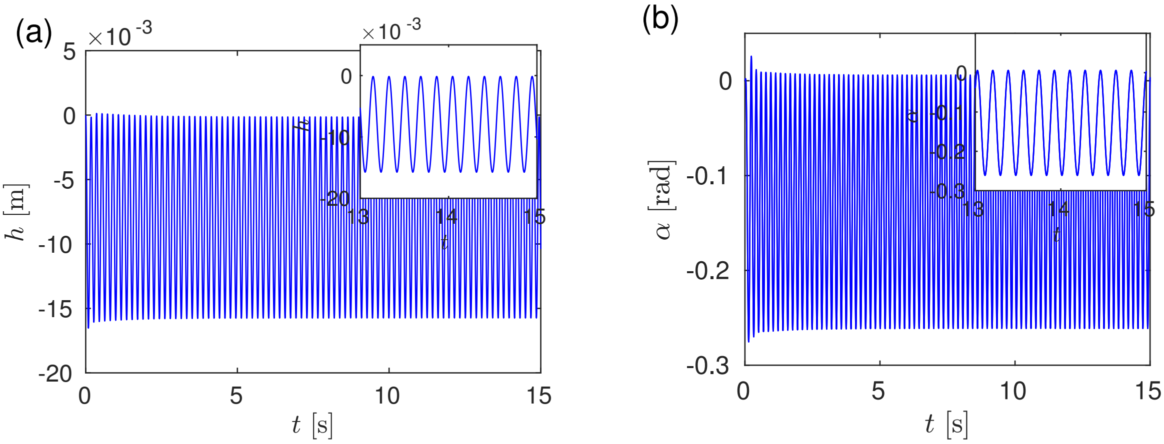

Figure 4.4: a)Plunge movement, b) Pitch movement for $U^* = 8.8$ m/s, using multibody-CFD model.

To evaluate the models' response to structural nonlinearities, a cubic nonlinear stiffness (δ) was introduced into the plunge degree of freedom (Case II). Figure 4.5 shows flutter velocity (U^*) as function of δ for both models. Table 4.1 also shows a comparison between flutter velocity for both cases. The multibody-CFD model consistently predicts a higher flutter velocity than the simplified model across the range of δ values. Furthermore, the LOM-Dowell model demonstrates greater sensitivity to changes in the nonlinear stiffness, exhibiting significantly larger percentage increases in flutter velocity compared to the multibody-CFD model. Despite these quantitative differences, both models show the same qualitative trend: an increase in the cubic stiffness leads to an increase in the flutter velocity.

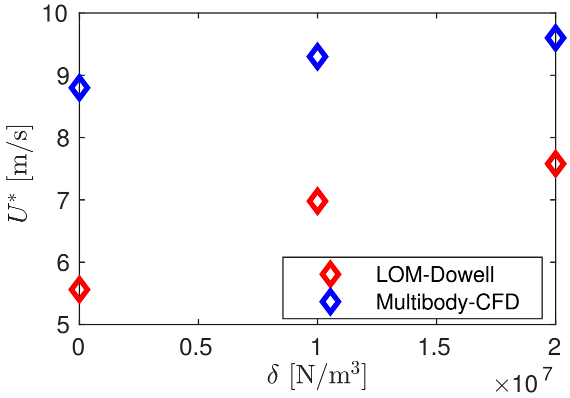

Figure 4.5: Flutter velocity as function of cubic nonlinear coefficient (δ), blue for simplified model and red for multibody model.

Table 4.1: Flutter velocity as function of δ for simplified and multibody models

δ	LOM-Dowell Model		Multibody-CFD Model	
δ [N/m^3]	U^* [m/s]	Relative Increase	U^* [m/s]	Relative Increase
$\delta = 0$	5.56	-	8.8	-
$\delta = 1 \times 10^7$	6.98	25.5%	9.3	5.7%
$\delta = 2 \times 10^7$	7.58	36.3%	9.6	9.1%

4.2 Moment and lift as function of angle of attack

The aerodynamic lift and moment at the respective flutter velocities were tracked for both models and Case I. Figure 4.6 illustrates the moment and lift as a function of the pitch angle, α. For the LOM-Dowell model, these relationships are represented by first-order lines. Notably, the moment for this model is null, a consequence of placing the airfoil's elastic axis at the aerodynamic center in the quasi-steady formulation. In contrast, the multibody-CFD model captures more complex aerodynamic phenomena. The lift force, defined as the combination of traditional lift and the drag component resulting from plunge motion, exhibits significant hysteresis, as does the aerodynamic moment. This elliptical behavior, captured by the URANS simulation, is a key feature of the unsteady fluid-structure interaction not present in the LOM-Dowell model.

Figure 4.7 shows moment and lift as function of angle of attack (α) for Case II. The inclusion of nonlinear cubic stiffness (δ) can increase the flutter velocity as it has the potential to decrease the amplitude. The inclusion of nonlinear cubic stiffness shifts lift

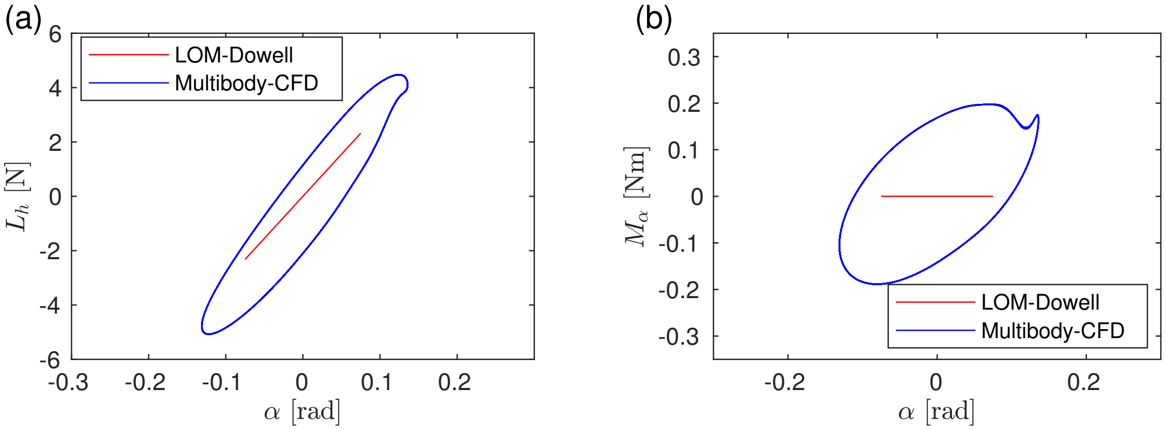

Figure 4.6: Lift and Moment for LOM-Dowell and multibody-CFD models. Adapted from Amaral et al. (2024).

and moment down in the vertical axis.

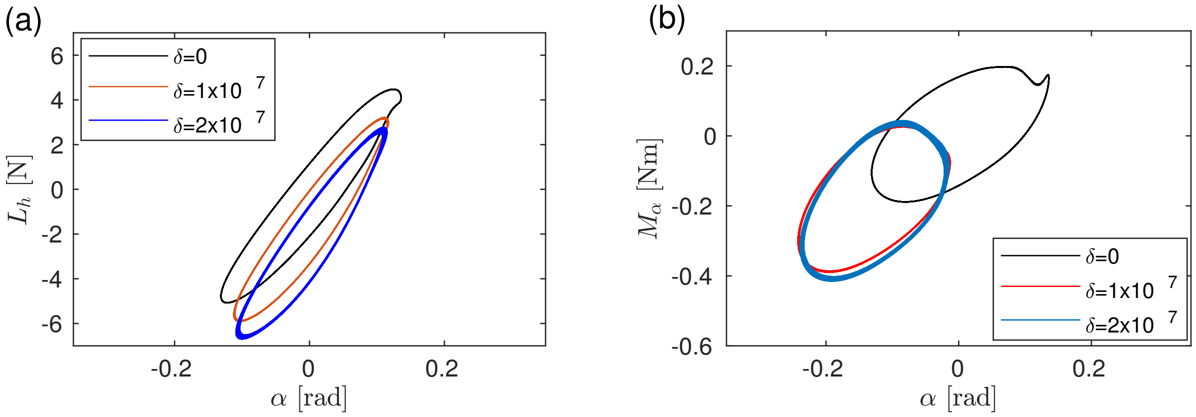

Figure 4.7: a) Lift and b)Moment for multibody-CFD model varying δ.

In summary, the validation of the LOM-Dowell model against the multibody-CFD model revealed a reasonable agreement in the predicted resonance frequency and the qualitative trend of flutter velocity as a function of the nonlinear stiffness, δ. Although the multibody-CFD model predicts a higher flutter velocity and captures more complex aerodynamic phenomena like hysteresis, the LOM-Dowell model provides qualitatively and, within certain margins, quantitatively consistent predictions. The observed differences underscore the importance of accounting for physical complexity in multibody-CFD model. Nonetheless, this comparison validates the LOM-Dowell model as an tool for the parametric uncertainty analyses and initial investigations of aeroelastic behaviour that are the focus of this paper.

Chapter 5

Energy harvesting performance

This chapter initiates with the analytical determination of the system's response utilizing the Multiple Scales Method (MMS). The analytical investigation utilizing MMS was performed specifically for Case IV of the system model. Subsequently, an analysis is performed to quantify the influence of nonlinear terms on the amplitude of the limit cycle and the resulting Hopf bifurcation. This analysis is validated numerically using the fourth-order Runge-Kutta method (RK). For both the MMS and the RK, the analysis focuses on varying the values of the parameters δ and K to thoroughly explore their influence on the system's dynamic response (LCOs/bifurcation) for Case IV. Finally, this chapter characterizes the fundamental dynamical behaviour of the aeroelastic system integrated with the Piezoelectric Nonlinear Energy Sink (PNES). A parameter sensitivity study is first conducted to identify the influence of nonlinear terms (δ and K) and key electrical parameters on flutter velocity and harvested power. As mention before, in a nonlinear context, the flutter speed is defined as the critical velocity at which the system transitions from a stable equilibrium point to a sustained amplitude of the limit cycle.

5.1 Multiple scale formulation

As described in chapter 2, MMS is an analytical method for calculating the response of the system near a center or focus, but to apply MMS in eq.(3.1), it can not present modulus, therefore Fourier Series is used to substitute the modulus. Applying Fourier Series, $|h|$ can be written in the form:

$$|h| = \frac{\pi}{2} - \frac{4}{\pi}\sum_{n=1}^{\infty}\frac{\cos(2n-1)h}{(2n-1)^2} \tag{5.1}$$

in which 5 terms are used, to find a satisfactory approximation.

When the modulus of the quadratic nonlinear term of the pizoelectric coupling is replaced by Fourier series, the equation presents $\cos(h)$. In the multiple scale method, it is necessary to replace the $\cos(h)$, it can be done using the Taylor series. Applying Taylor Series, $\cos h$ has the following form:

$$\cos(h) = 1 - \frac{h^2}{2!} + \frac{h^4}{4!} - \frac{h^6}{6}... \tag{5.2}$$

After apply Fourier Series and Taylor Series, the eq. (3.1) is ready to be manipulated with MMS. The first step to start MMS is to determine the matrices of mass, stiffness and damping and the vectors of nonlinearity of eq. (3.1):

$$M_m = \begin{bmatrix} m + m_e & bmx_\alpha & 0 \\ bmx_\alpha & I_\alpha & 0 \\ 0 & 0 & L \end{bmatrix} \tag{5.3}$$

$$C_m = \begin{bmatrix} 2U^* b\pi\rho + d_h & 0 & 0 \\ -2U_f b^2 \pi\rho e & d_\alpha & 0 \\ 0 & 0 & R \end{bmatrix} \tag{5.4}$$

$$K_m = \begin{bmatrix} k_h & 2U_f^2 b\pi\rho & \frac{-99225K\Theta\pi^2+198450\Theta\pi-939752K\Theta}{198450C_p\pi} \\ 0 & k_\alpha - 2U_f^2 b^2\pi\rho e & 0 \\ \frac{-99225K\Theta\pi^2+198450\Theta\pi-939752K\Theta}{198450C_p\pi} & 0 & 1/C_p \end{bmatrix} \tag{5.5}$$

$$G_c = \begin{bmatrix} \delta h^3 - \frac{10K\Theta h^2 q}{C_p\pi} \\ 0 \\ -\frac{10K\Theta h^3}{C_p\pi} \end{bmatrix} \tag{5.6}$$

in which U^* is the flutter speed. It is possible to notice the influence of the quadratic nonlinear term K in the linear stiffness matrix.

The state variables are:

$$Y = \begin{bmatrix} h \\ \alpha \\ q \\ \dot{h} \\ \dot{\alpha} \\ \dot{q} \end{bmatrix} \tag{5.7}$$

Thus, the equations are written in the form:

$$\dot{Y} = A(U)Y \tag{5.8}$$

The matrix $A(U)$ can be given by:

$$A(U) = \begin{bmatrix} 0_{3x3} & I_{3x3} \\ -MK^{-1} & -MC^{-1} \end{bmatrix} \tag{5.9}$$

Tha matrix B is determined by matrix $A(U)$. We must substitute $U^* = U^* + \epsilon^2\sigma_u$ in matrix $A(U)$ and use all elements that multiply ϵ^2:

$$B = \begin{bmatrix} 0 & 0 & 0 & 0 & 0 & 0 \\ 0 & 0 & 0 & 0 & 0 & 0 \\ 0 & 0 & 0 & 0 & 0 & 0 \\ 0 & \frac{(4U^*b^3m\pi\rho\sigma_u x_\alpha^2+4I_\alpha U^*b\pi\rho\sigma_u)}{(b^2m^2x_\alpha^2-I_\alpha m_e-I_\alpha m)} & \frac{(2b^3m\pi\rho\sigma_u x_\alpha e+2I_\alpha b\pi\rho\sigma_u)}{(b^2m^2x_\alpha^2-I_\alpha m_e-I_\alpha m)} & 0 & 0 & 0 \\ 0 & -\frac{(4\pi U^*b^2m_e+4\pi U^*b^2m)\rho\sigma_u e+4U^*b^2m\pi\rho\sigma_u x_\alpha}{(b^2m^2x_\alpha^2-I_\alpha m_e-I_\alpha m)} & -\frac{(2\pi b^2m_e+2\pi b^2m)\rho\sigma_u e+2b^2m\pi\rho\sigma_u x_\alpha}{(b^2m^2x_\alpha^2-I_\alpha m_e-I_\alpha m)} & 0 & 0 & 0 \\ 0 & 0 & 0 & 0 & 0 & 0 \end{bmatrix} \tag{5.10}$$

The eigenvectors of eq. (5.9) are also required in the method. The right eigenvector is represented by p, and the left eigenvector is represented by q_q which is normalized as:

$$q = \frac{q_q}{|q_q^T p|} \tag{5.11}$$

System response for the multiple scale method is given by:

$$a = \sqrt{\frac{-4\beta}{\Lambda_a}} \tag{5.12}$$

in which the parameters Λ_a and β are given by:

$$\Lambda_a = 3q_q^T C_c(p, p, \overline{p}) \tag{5.13}$$

$$\beta = q_q^T \sigma_u B p \tag{5.14}$$

5.2 Influence of nonlinear terms

Figure 5.1 and 5.2 shows Hopf bifurcation, that illustrates the qualitative change in the system, using RK and MMS. Linear studies typically analyze the system only up to the bifurcation point. When nonlinear terms are introduced, it becomes essential to observe the system's behaviour within the post-flutter regime. This region is critical because it represents the functional operating condition, enabling both the harvesting of energy and the suppression of amplitude of the limit cycle. Figure 5.1 uses $\delta = 1 \times 10^7$ N/m^3 and fig. 5.2 uses $\delta = 2 \times 10^7$ N/m^3, comparing both, it is possible to see that when we increase the value of δ, the amplitude decreases, for the same wind speed range. Comparing the increase of K for each method, mechanical amplitudes increase with MMS method, while plunge amplitude has a small decrease and pitch amplitude has a small increase with RK method, the electrical part of the system has the same behaviour of increasing for both methods when K increases. Therefore, the both methods agrees that increasing quadratic nonlinear electromechanical coupling increases amplitude of charge, which can increase power produced by energy harvesting. We can notice a relation between pitch and charge amplitudes, since pitch decreases and charge increases.

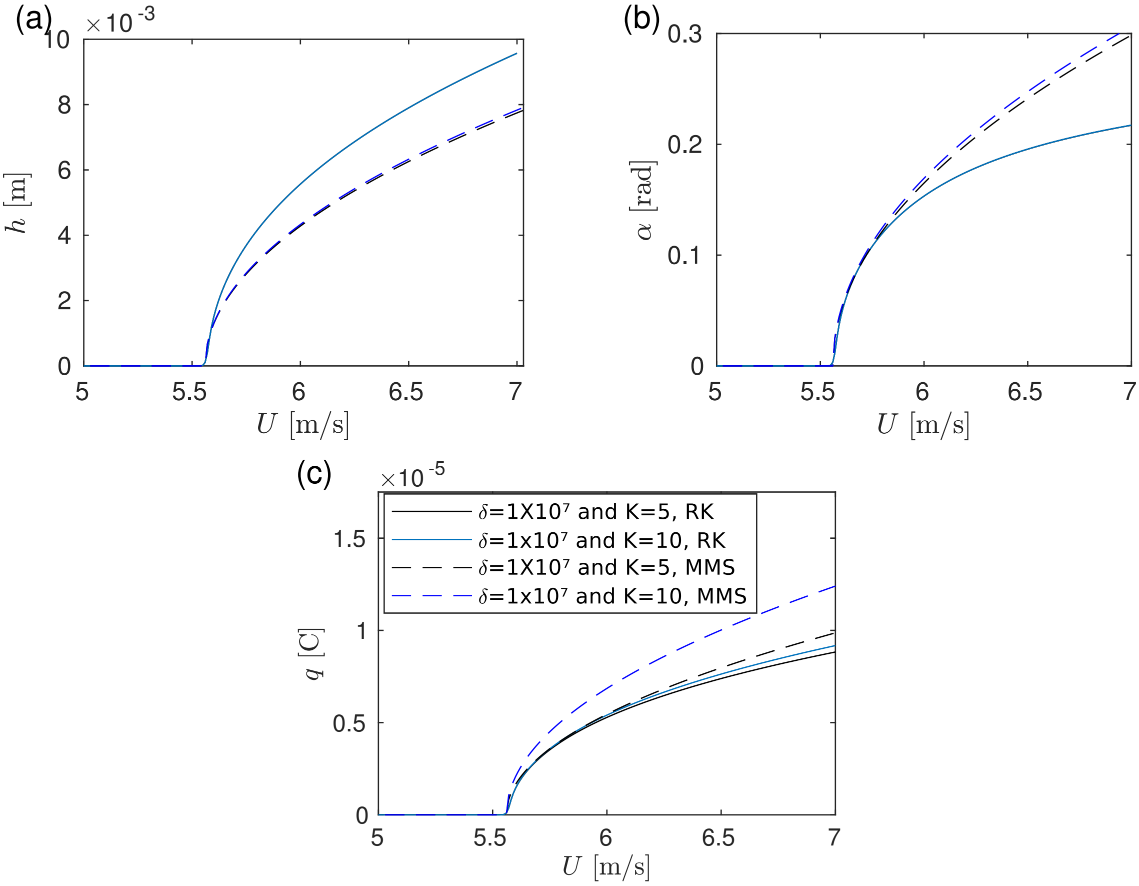

Figure 5.1: Hopf bifurcation with $\delta = 1 \times 10^7$ N/m^3 for a) plunge, b) pitch and c) charge.

The influence of nonlinear terms δ and K in flutter velocity and in the harvest power are also investigated. The values of nonlinear terms varying from $\delta = 0$ to $\delta = 2 \times 10^7$ N/m^3 and from $K = 0$ to $K = 100$. Figures 5.3 and 5.4 show flutter velocity, mechanical power (plunge and pitch) and electrical power as function of δ for five values of K, and as function of K for five values of δ. The flutter velocity increases quickly until approximately $\delta = 1 \times 10^7$ N/m^3, after this value the flutter velocity stabilizes. Mechanical power (plunge and pitch) increases until $\delta = 0.3 \times 10^7$ N/m^3 and then decreases. Electrical power has the same trend of mechanical power. The quadratic nonlinear electromechanical coupling coefficient (K) decreases U^* slowly. Mechanical power does not suffer much influence from K, but electrical power increases

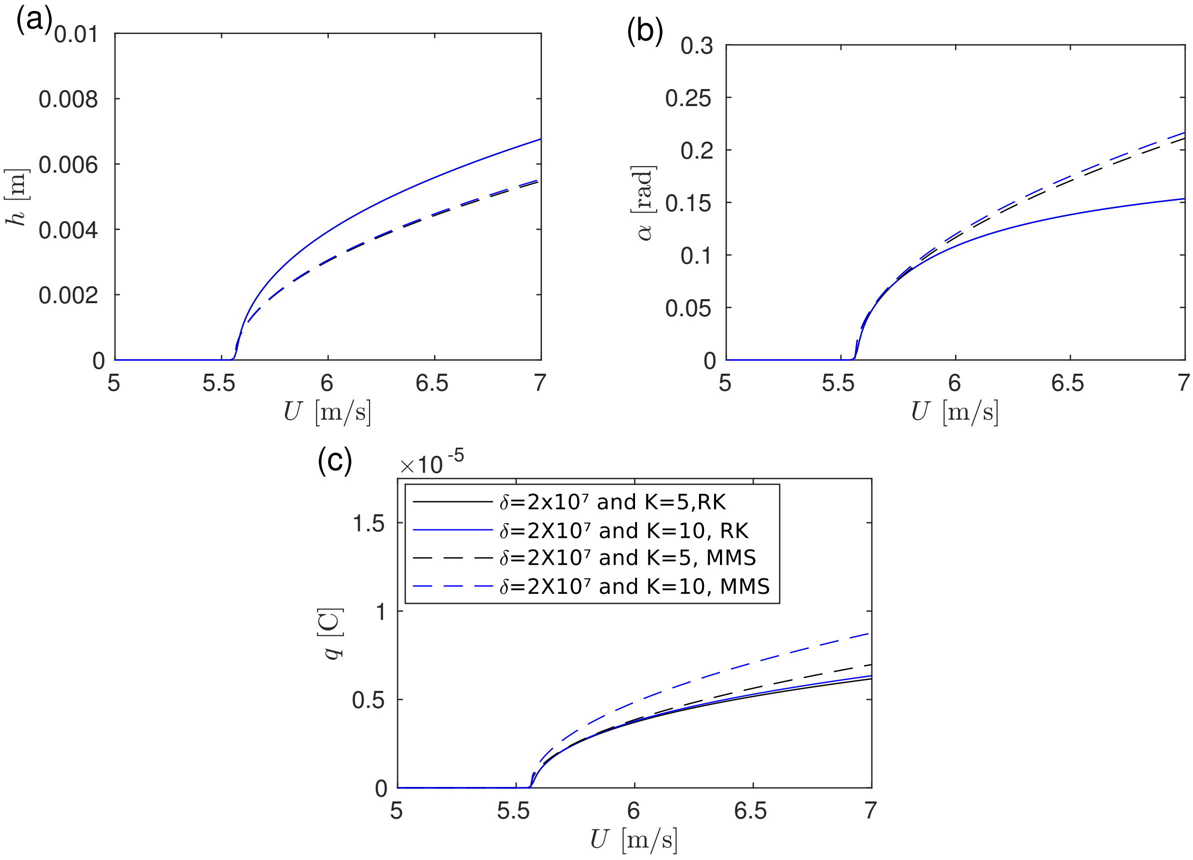

Figure 5.2: Hopf bifurcation with $\delta = 2 \times 10^7$ N/m^3 for a) plunge, b) pitch and c) charge

when K increases. δ influences U^* more than K, and K influences mainly P_e, it is capable of increase P_e which is the most important topic to make energy harvesting viable. δ increases flutter velocity but decreases mechanical and electrical power, due the decrease in the amplitude response. The biggest power harvested happens for the biggest value of K and smallest value of δ.

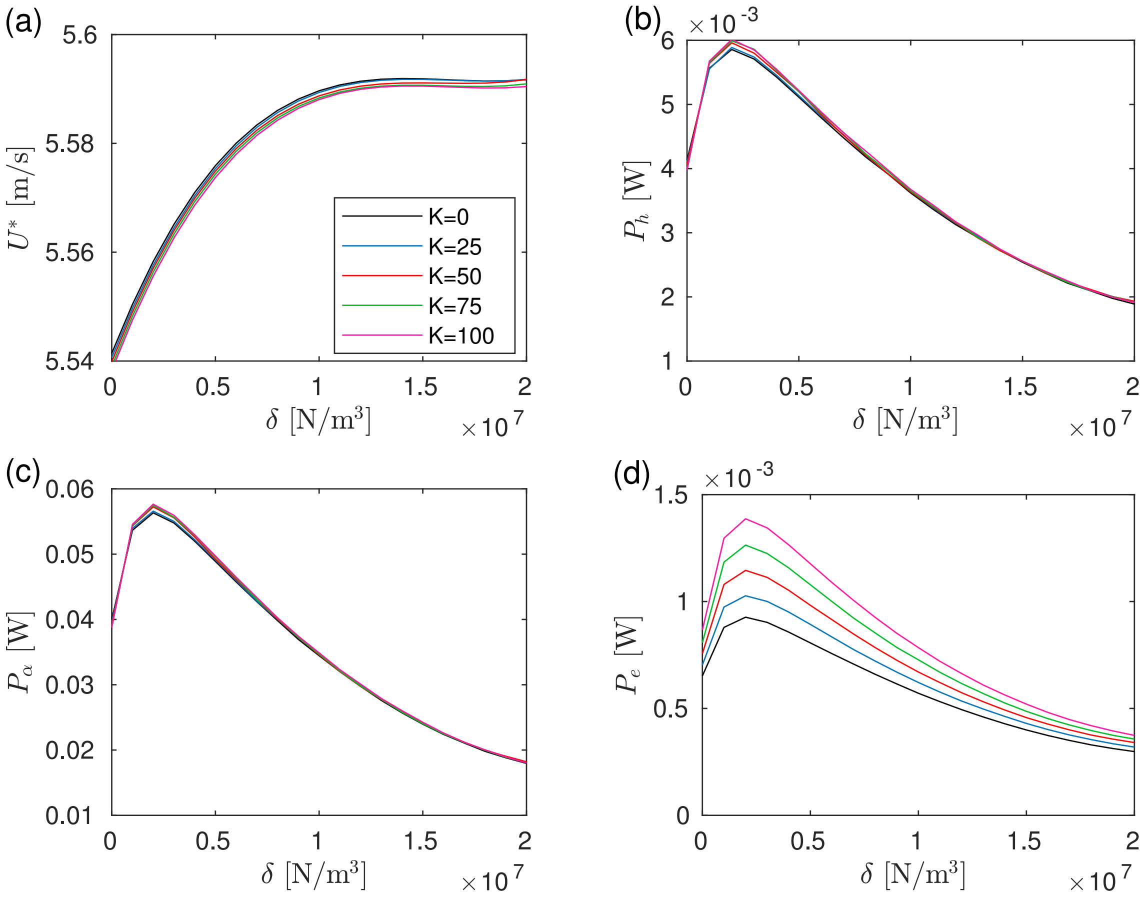

Figure 5.3: a) Flutter velocity b) Mechanical power related to plunge c) Mechanical power related to pitch d) Electrical power as function of δ, for five values of K.

5.3 Influence of electrical parameters

The influence of the primary electrical parameters - linear electromechanical coupling (θ), resistance (R), capacitance (C_p), and inductance (L) - on the critical flutter velocity (U^*) and the harvested electrical power was investigated. Figure 5.5 illustrates these

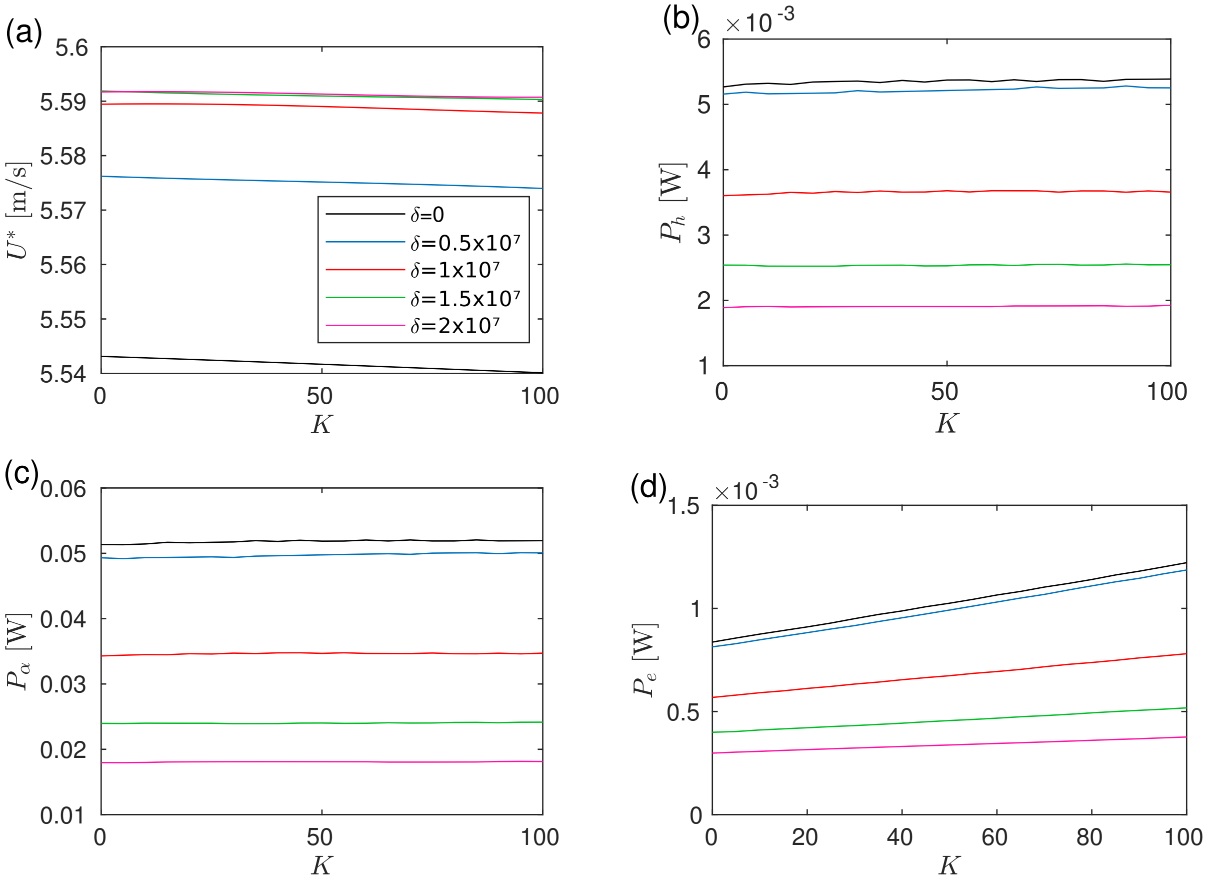

Figure 5.4: a) Flutter velocity b) Mechanical power related to plunge c) Mechanical power related to pitch d) Electrical power as function of K, for five values of δ.

relationships, with the parameter ranges normalised to facilitate direct comparison.

The analysis reveals a inverse correlation between the linear piezoelectric coupling (θ) and the flutter velocity (U^*), where an increase in θ leads to a lower flutter onset velocity. Conversely, the electrical power harvested by the PNES is significantly enhanced by increasing θ, underscoring its critical role in the energy conversion process. A similar, though less pronounced, trend is observed for the quadratic coupling term, K. In contrast, increasing the electrical resistance (R) leads to a monotonic decrease in both flutter velocity and electrical power. Furthermore, the system exhibits a distinct optimal operational point with respect to capacitance (C_p), where both flutter velocity and harvested power reach a minimum value around a normalized capacitance of 0.5. Note that C_p does not influence the system as much as θ, although both parameters contribute to the overall stiffness, This can be explain because C_p appears isolated within the electrical domain equations, whereas θ acts as a coupling term between the mechanical and electrical subsystems. The inductance (L) was found to have a negligible impact on both the critical flutter velocity and the electrical power within the tested range. These findings establish that the piezoelectric coupling parameter, θ, is the most influential factor in determining the power generation capabilities of the PNES.

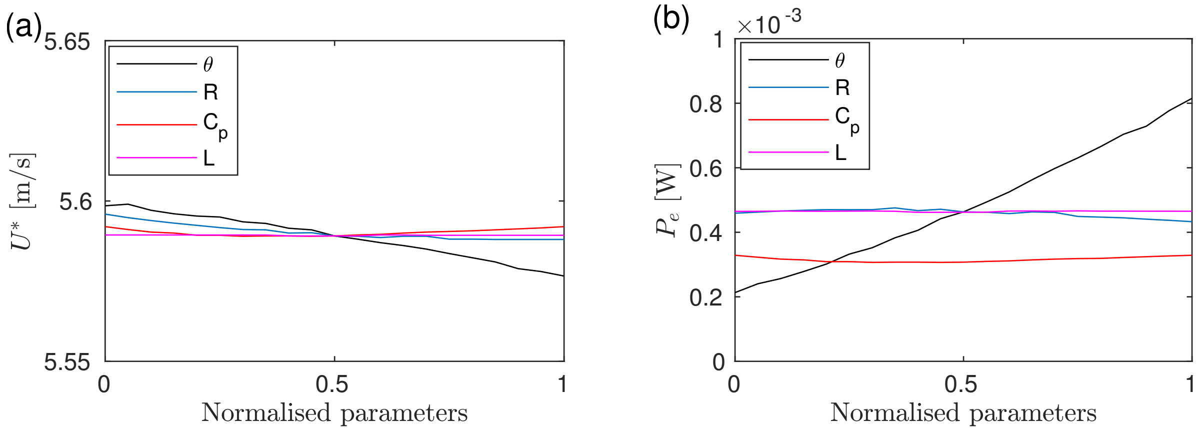

Figure 5.5: a) Flutter velocity b) Electrical power as function of normalised electrical parameters, θ, R, C_p and L.

Chapter 6

Robustness assessment of PNES

In the context of energy harvesting, robustness is defined as the system's ability to maintain stable performance despite parameter fluctuations; thus, a significantly lower variance indicates higher robustness. A deterministic analysis was performed to provide a preliminary assessment of system robustness, highlighting the complexities that motivate a more rigorous probabilistic approach. Then, the deterministic analysis of the preceding section was complemented by a probabilistic uncertainty analysis. A Monte Carlo Simulation (MCS) was conducted to compare the robustness of the linear (Case III) and nonlinear (Case IV) systems by examining the statistical distribution of the harvested electrical power. Two levels of uncertainty were investigated by setting the coefficient of variation for the input parameters (λ_i) to 5% and 15%, with each parameter defined by an independent normal distribution. This section presents the analysis of both the transient and steady-state power responses.

6.1 Deterministic robustness analysis

To perform a preliminary assessment of robustness, the system's response to variations in the most influential electrical parameters (θ, R, and C_p) was analysed. The transient average power (P_e) was calculated as a function of wind velocity (U) for three values of each parameter: a nominal value, a lower value, and a higher value. The results for the linear system (Case III) and the nonlinear system with PNES (Case IV) are compared in Fig. 6.1.

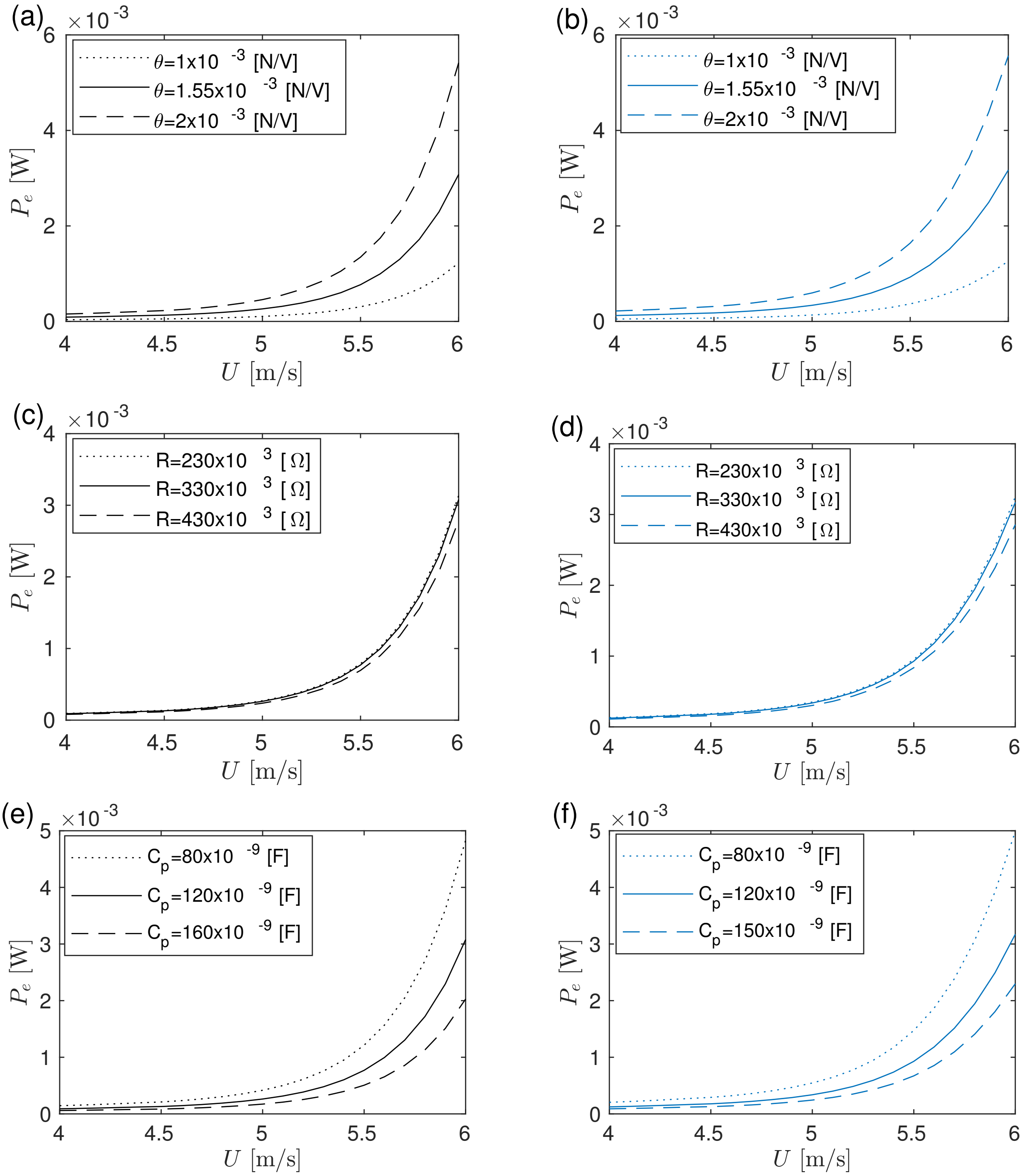

Figure 6.1: Electrical power as function of wind velocity (U), for θ R and C_p a), c), e) Case III and b), d), f) Case IV.

To quantitatively compare the sensitivity, a ratio (R_n) was defined as:

$$R_n = \frac{|A_d - A_p|}{A_s} \tag{6.1}$$

in which A_d, A_p and A_s are the areas under the respective power-velocity curves for the higher, lower, and nominal parameter values. This ratio serves as an indicator of the sensitivity of P_e to variations in a given electrical parameter.

The calculated values for R_n are presented in Table 6.1. For variations in θ, the sensitivity ratio R_n increases when the nonlinear terms are included (Case IV). This is expected, as θ is a primary driver of electrical power. In contrast, for variations in R and C_p, the sensitivity ratio decreases in the presence of the PNES. This suggests that the nonlinear system is more robust to variations in its passive electrical components.

This analysis was repeated using the steady-state average power per cycle (P_e), as shown in Figure 6.2 and Tables 6.2 and 6.3. The results corroborate the findings from the transient analysis. For variations in R and C_p, the linear system (Case III) exhibits a larger variation in output power, indicating that the nonlinear system (Case IV) is indeed more robust.

Table 6.1: R_n for electrical power curves in fig. 6.1.

Region	Case	θ [N/V]	R [Ω]	C_p [F]
R_n	III	1.3518	0.0833	0.9253
	IV	1.3897	0.07143	0.8571

The deterministic results present a complex picture. While the PNES enhances robustness against variations in passive electrical components, the system's sensitivity to the primary electromechanical coupling parameter increases. These observations underscore the limitations of one-parameter-at-a-time sensitivity studies for evaluating the overall robustness of a complex, coupled nonlinear system. The interplay between parameters and the wind velocity regime makes a definitive conclusion based on this approach challenging.

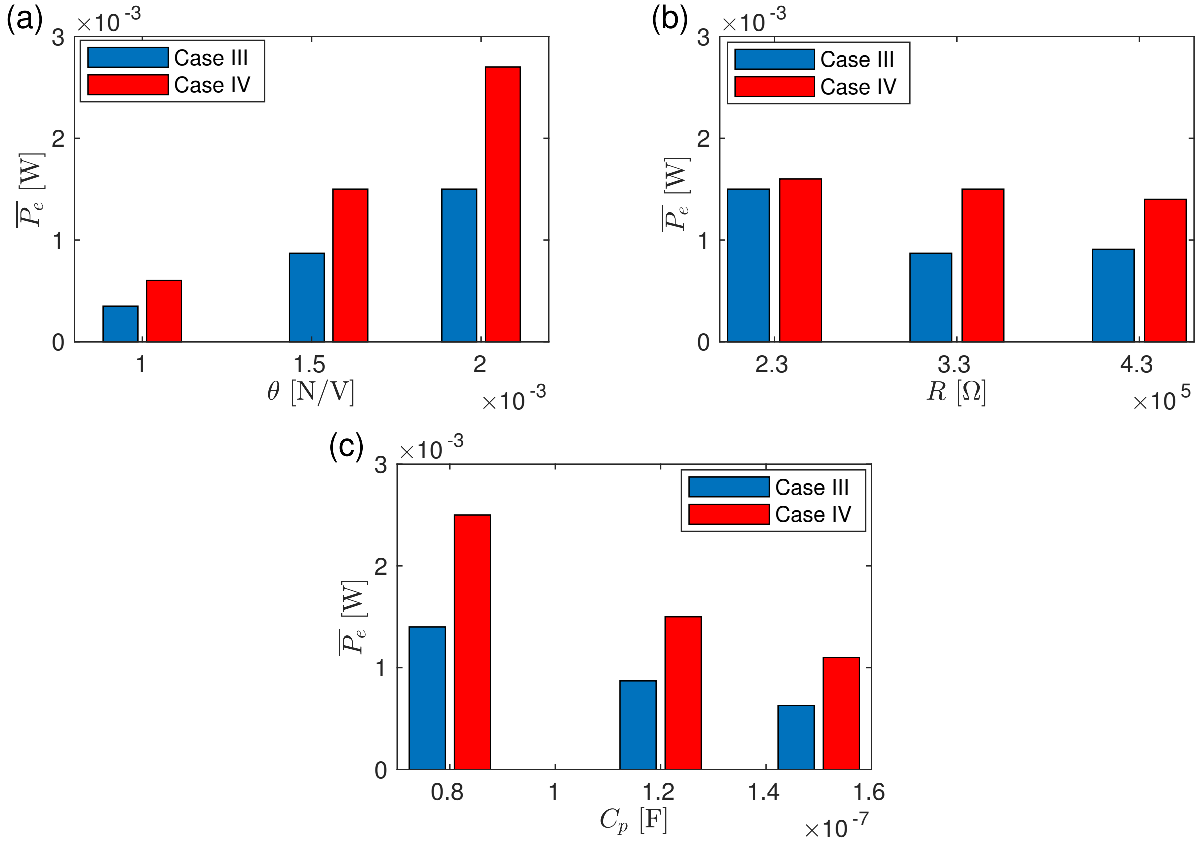

Figure 6.2: Electrical power as function of θ, R and C_p in steady state for Case III and Case IV.

Table 6.2: Flutter and electrical power in steady state for determined values of θ, R and C_p - Case III.

Situation	U^* [m/s]	$\overline{P_e}$ [W]	
Value	Value	Value $\times 10^{-4}$	Relative increase %
Nominal	5.5432	8.7021	-
$\theta = 1 \times 10^{-3}$ N/V	5.5515	3.5028	-59.75
$\theta = 2 \times 10^{-3}$ N/V	5.5337	15.000	72.37
$R = 230 \times 10^3\ \Omega$	5.5485	9.0904	4.50
$R = 430 \times 10^3\ \Omega$	5.5418	7.6952	-11.57
$C_p = 80 \times 10^{-9}$ F	5.5454	14.000	60.88
$C_p = 150 \times 10^{-9}$ F	5.5450	6.2852	-27.77

Table 6.3: Flutter and electrical power in steady state for determined values of θ, R and C_p - Case IV.

Situation	U^* [m/s]	$\overline{P_e}$ [W]	
Value	Value	Value $\times 10^{-4}$	Relative increase %
Nominal	5.7039	15.000	-
$\theta = 1 \times 10^{-3}$ N/V	5.7068	6.0344	-95.98
$\theta = 2 \times 10^{-3}$ N/V	5.7022	27.000	80.00
$R = 230 \times 10^3\ \Omega$	5.7149	16.000	6.67
$R = 430 \times 10^3\ \Omega$	5.6997	14.000	-6.67
$C_p = 80 \times 10^{-9}$ F	5.7214	25.000	66.67
$C_p = 150 \times 10^{-9}$ F	5.7017	11.000	-26.67

Therefore, to provide a more comprehensive and statistically meaningful assessment of system robustness, a probabilistic uncertainty analysis is performed in the following section. This approach allows for the simultaneous variation of multiple parameters and provides a clearer, more integrated perspective on the system's performance under uncertainty.

6.2 Uncertainty robustness analysis

The primary metric used to quantify the variability of the transient average power (P_e) and, consequently, the system's robustness is the output coefficient of variation (λ_o). Figure 6.3 shows that for a low level of input uncertainty ($\lambda_i = 5\%$), the robustness of Case III and Case IV is comparable, with nearly identical λ_o values. However, at a higher level of uncertainty ($\lambda_i = 15\%$), a significant divergence occurs: λ_o for Case III trends sharply upward post-flutter, while for Case IV it remains subdued, confirming the superior robustness of the nonlinear system.

This conclusion is supported by the Kernel Density Estimate (KDE) plots in Figure 6.4, which visualize the distribution of P_e. For both cases, the mean and median values are in close proximity, suggesting largely symmetrical datasets. Critically, when $\lambda_i = 15\%$, the distribution for Case IV exhibits less dispersion, reinforcing its enhanced

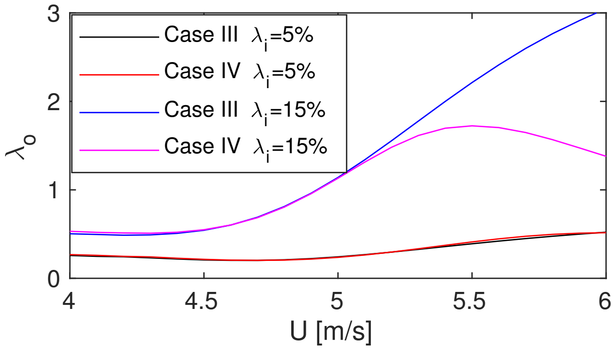

Figure 6.3: Coefficient of variation of P_e (λ_o) as function of U for cases III and IV.

robustness.

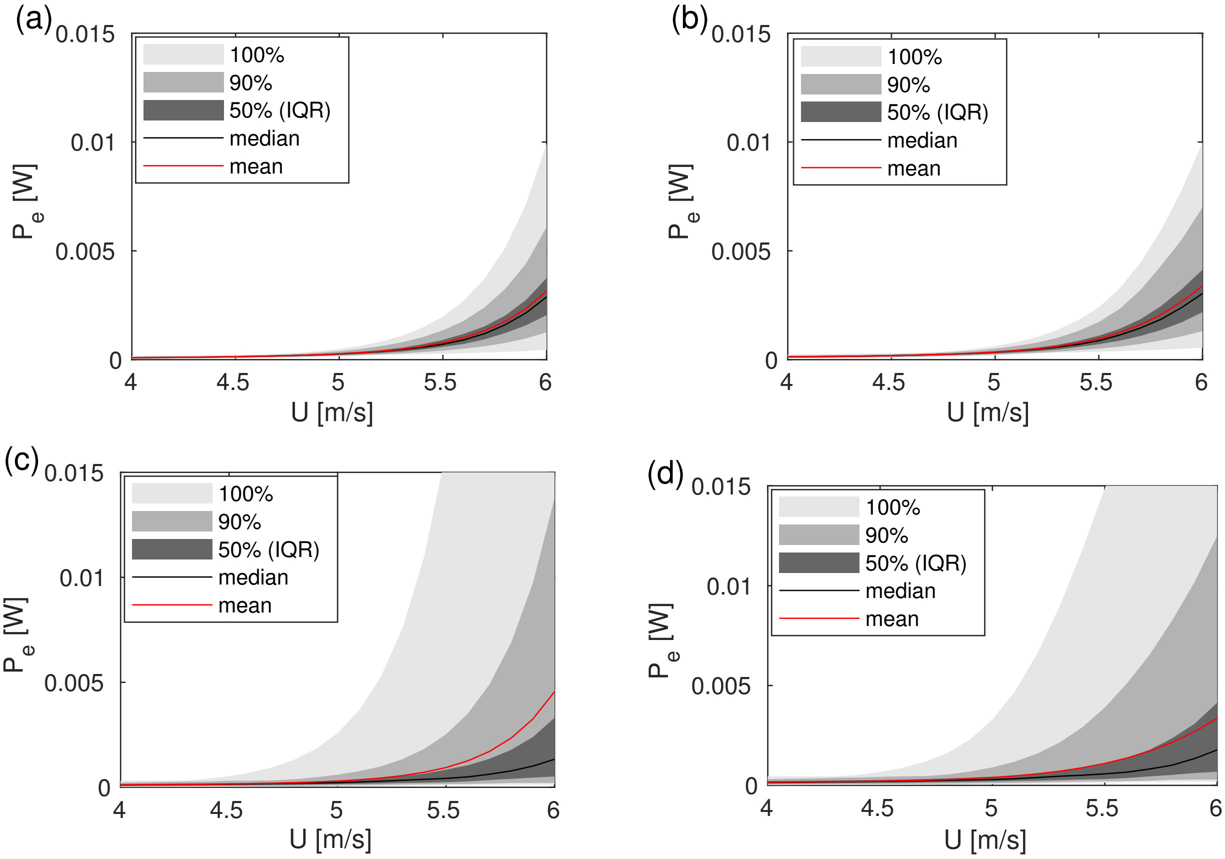

Figure 6.4: Kernel Density Estimate (KDE) plots related to quantiles 100%, 90% and 50% (inter quartil region), the meridian and the mean, in which a) Case III with $\lambda_i = 5\%$, b) Case II with $\lambda_i = 5\%$, c) Case I with $\lambda_i = 15\%$ and d) Case IV with $\lambda_i = 15\%$.

The analysis of the steady-state average power per cycle ($\overline{P_e}$), presented as boxplots in Figure 6.5, corroborates these findings. The normalized results, in particular, show that Case IV exhibits significantly less data dispersion than Case III when subjected to a 15% input uncertainty, providing further evidence of its superior robustness. To corroborate this result, a one-sided Ansari-Bradley test was conducted with a significance level of 0.05. The Ansari-Bradley test is a non-parametric statistical procedure employed to compare the scale parameters (dispersion) of two independent samples. The test concluded that Case IV has smaller variance compared to Case III for $\lambda_i = 15\%$.

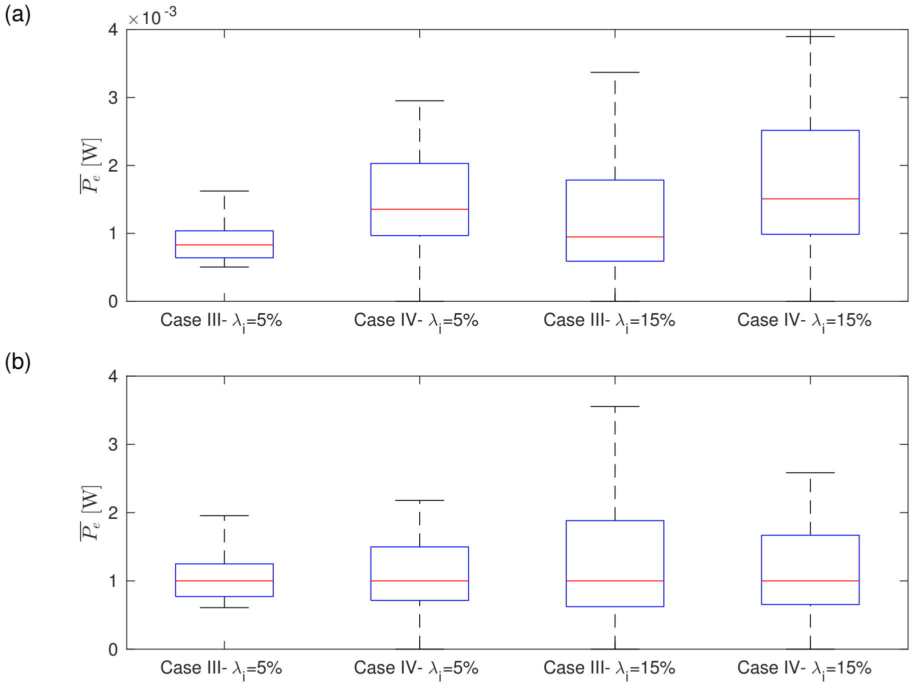

Figure 6.5: P_e distribution for steady state regime with a) original scale values and b) normalised values.

6.3 Statistical distribution of harvested power

The statistical nature of the power distribution was further investigated using histograms, kurtosis, and skewness. For the transient response (Figure 6.6), the distributions become more tapered and less symmetric as input uncertainty increases. This is quantified in Figure 6.7, which shows that both kurtosis (peakedness) and skewness (asymmetry) increase with a higher λ_i. The nonlinear case with $\lambda_i = 15\%$ exhibits the highest values for both metrics.

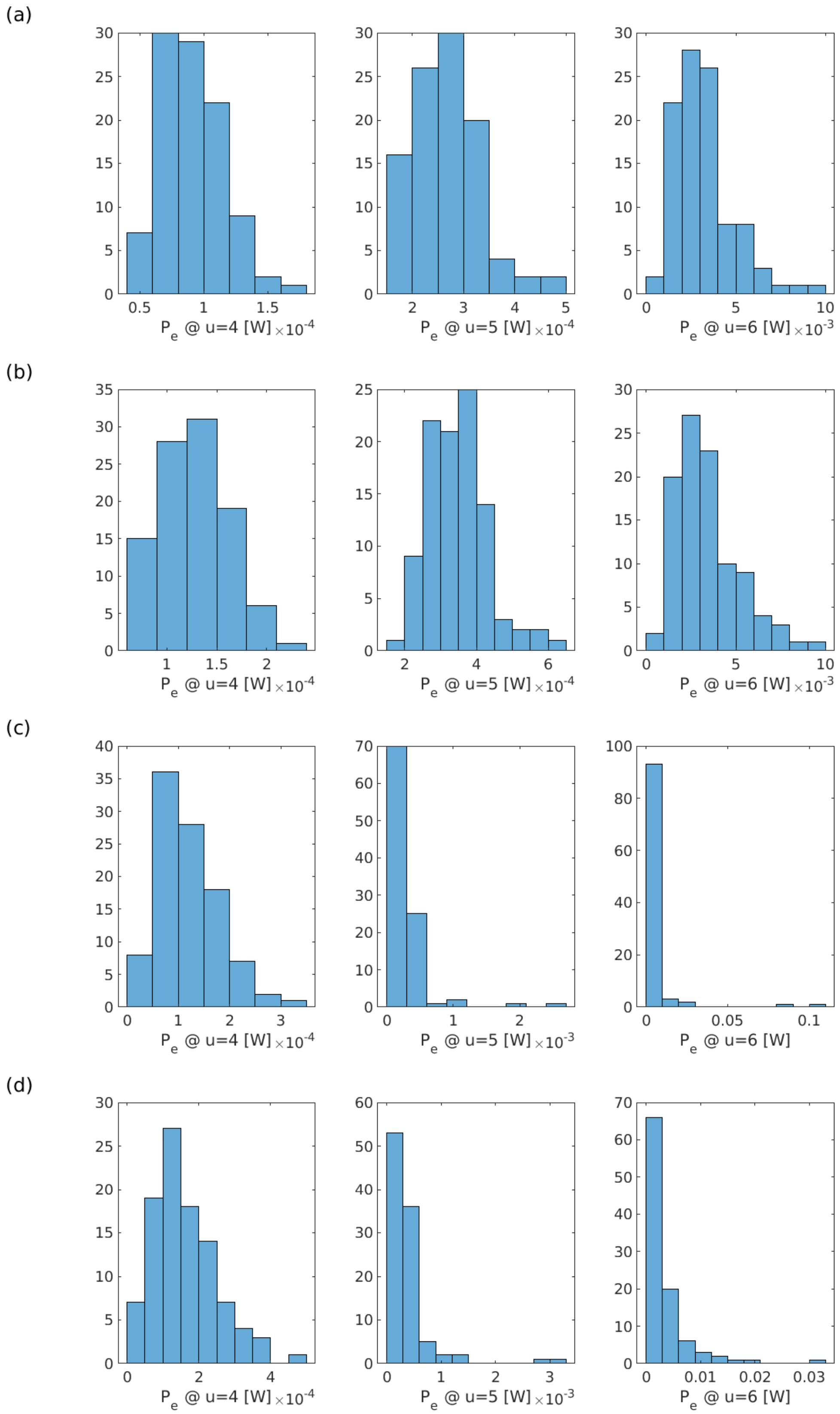

Figure 6.6: Histograms of electrical power for three value ranges of U, a) Case III with $\lambda_i = 5\%$, b) Case IV with $\lambda_i = 5\%$, c) Case III with $\lambda_i = 15\%$ and d) Case IV with $\lambda_i = 15\%$.

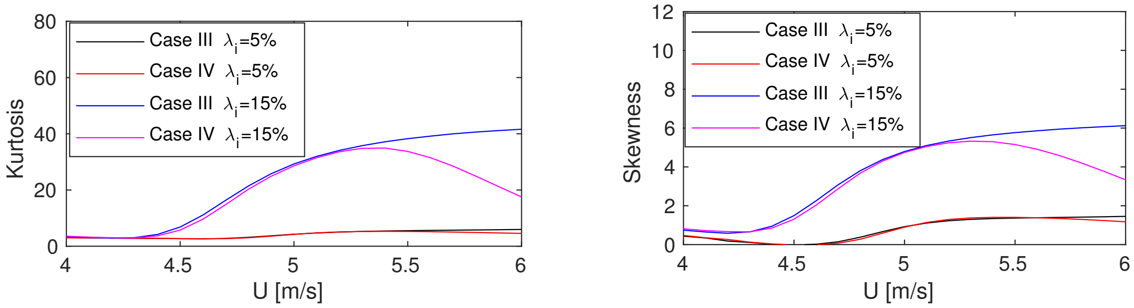

Figure 6.7: a) Kurtosis for Case III and Case IV b) Skewness for Case III and Case IV.

A similar analysis for the steady-state response (Figure 6.8) reveals the presence of a few high-power outliers, particularly for Case IV at $\lambda_i = 15\%$. As detailed in Table 6.4, the raw distribution for this scenario is highly asymmetrical and peaked. However, after excluding these outliers (fewer than 10 samples, identified as not aligning with deterministic results), the distribution becomes substantially more symmetrical (Table 6.5). This indicates that the apparent asymmetry in the steady-state response of the nonlinear system was primarily driven by a small number of extreme-value events.

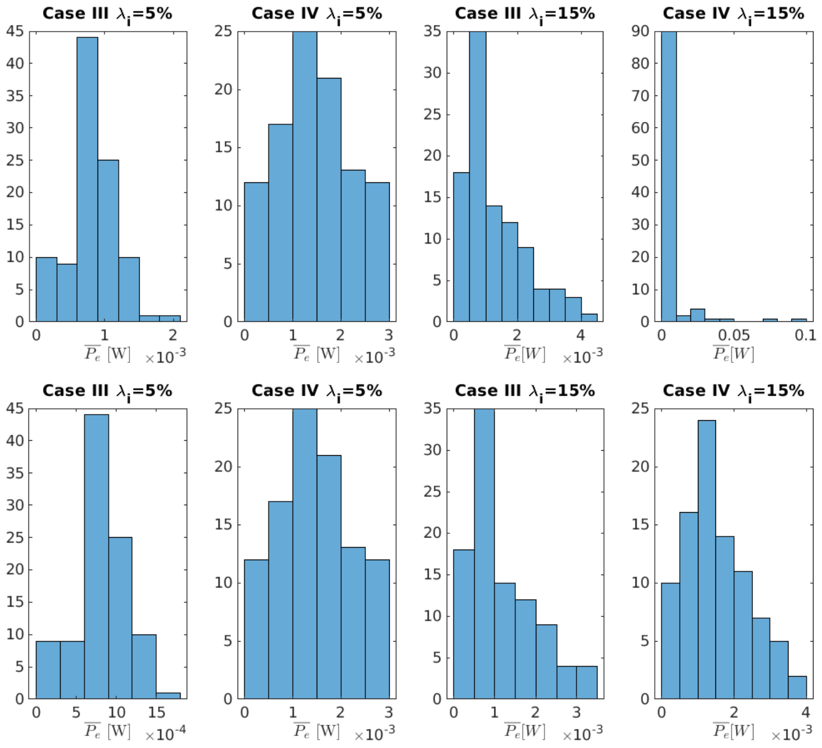

Figure 6.8: Histograms of electrical power for steady state regime with outliers and without outliers for cases III and IV, with $\lambda_i = 5\%$ and $\lambda_i = 15\%$.

Table 6.4: Skewness, Kurtosis and Coefficient of Variation of $\overline{P_e}$ (λ_o) for steady-state regime - with outliers.

Case	λ_i	Skewness	Kurtosis	λ_o
III	5%	-0.3440	3.8857	0.4598
	15%	1.1077	3.5588	0.7554
IV	5%	-0.1265	2.4054	0.5495
	15%	4.6658	26.5540	2.6054

Table 6.5: Skewness, Kurtosis and Coefficient of variation of $\overline{P_e}$ (λ_o) for steady-state regime - without outliers.

Case	λ_i	Skewness	Kurtosis	λ_o
III	5%	-0.6316	3.4204	0.4595
	15%	0.8785	3.0279	0.7439
IV	5%	-0.1265	2.4054	0.5495
	15%	0.3800	2.5170	0.7089

6.4 Parameter influence under uncertainty

To identify the most influential input parameters on the transient power output, both linear correlation coefficients (C_c) and multiple linear regression coefficients (Q) were calculated. The results, shown in Figures 6.9 and 6.10, are highly consistent. Both analyses identify the electromechanical coupling (θ) as having the largest positive correlation (direct relationship) and the plunge stiffness (k_h) as having the largest negative correlation (inverse relationship) with the electrical power. These findings confirm the deterministic results, highlighting θ and k_h as the dominant parameters influencing system performance under uncertainty.

6.5 Validation of the Monte Carlo simulation

The Confidence Interval (CI) of the mean is a range of values that is likely to contain the true population mean based on a sample of data. The sufficiency of the 100-sample size used for the MCS was validated by analyzing the CI of the mean transient power,

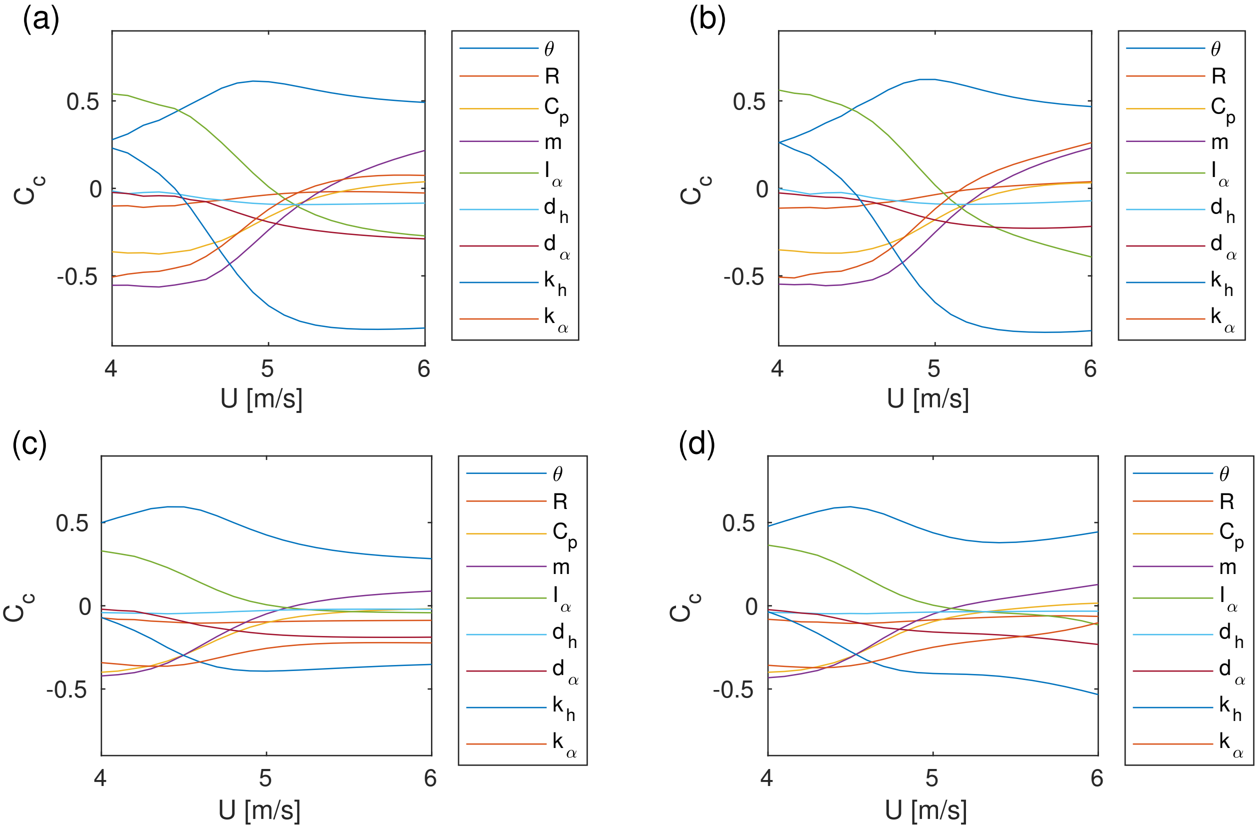

Figure 6.9: Correlation (C_c) between each of the input parameters and electrical power, a) Case III with $\lambda_i = 5\%$, b) Case IV with $\lambda_i = 5\%$, c) Case III with $\lambda_i = 15\%$ and d) Case IV with $\lambda_i = 15\%$.

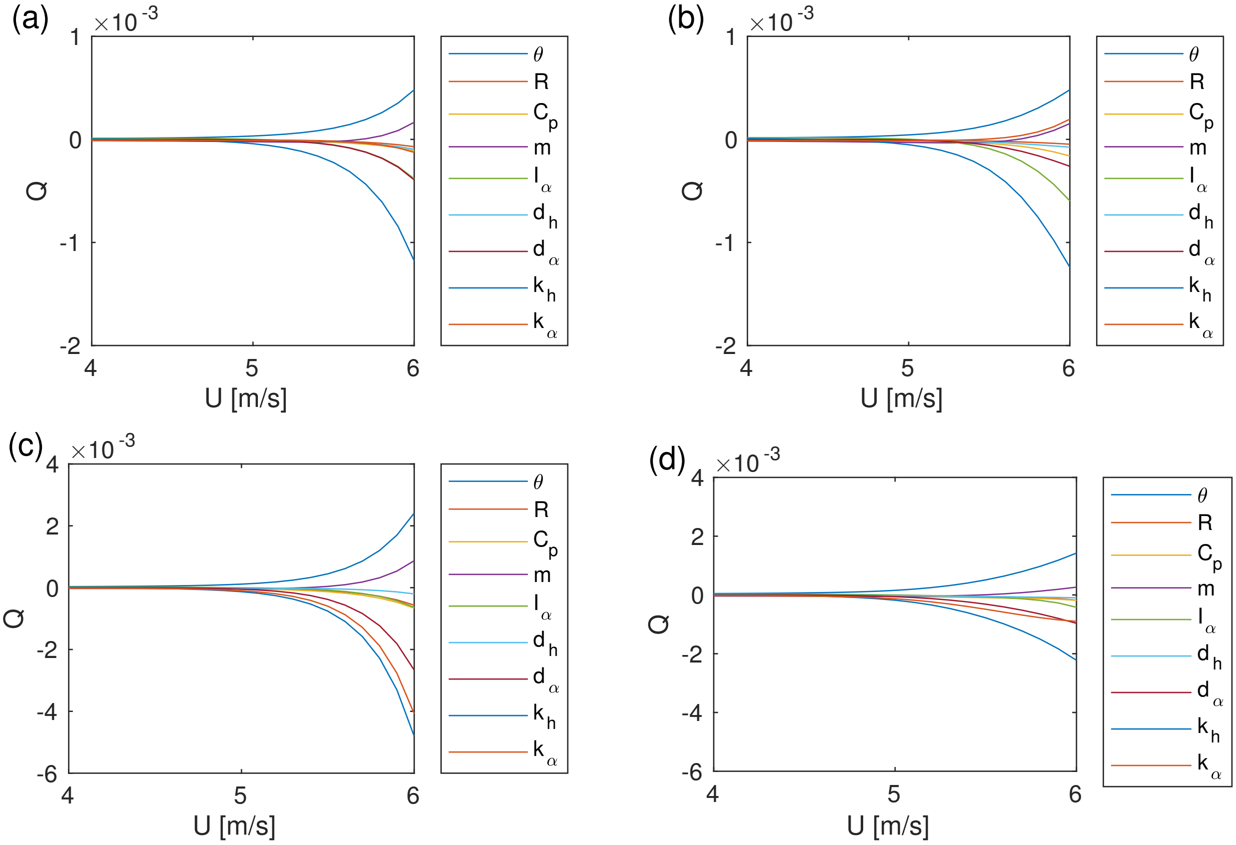

Figure 6.10: Regression coefficient (Q) a) Case III with $\lambda_i = 5\%$, b) Case IV with $\lambda_i = 5\%$, c) Case III with $\lambda_i = 15\%$ and d) Case IV with $\lambda_i = 15\%$.

as shown in Figure 6.11. The narrow bandwidth of the CI across the velocity range, with no considerable dispersion, demonstrates that the statistical results are stable and reliable. Also, an analysis using 200 samples yielded no significant changes compared to the 100-sample case, confirming the sufficiency of the original sample size.

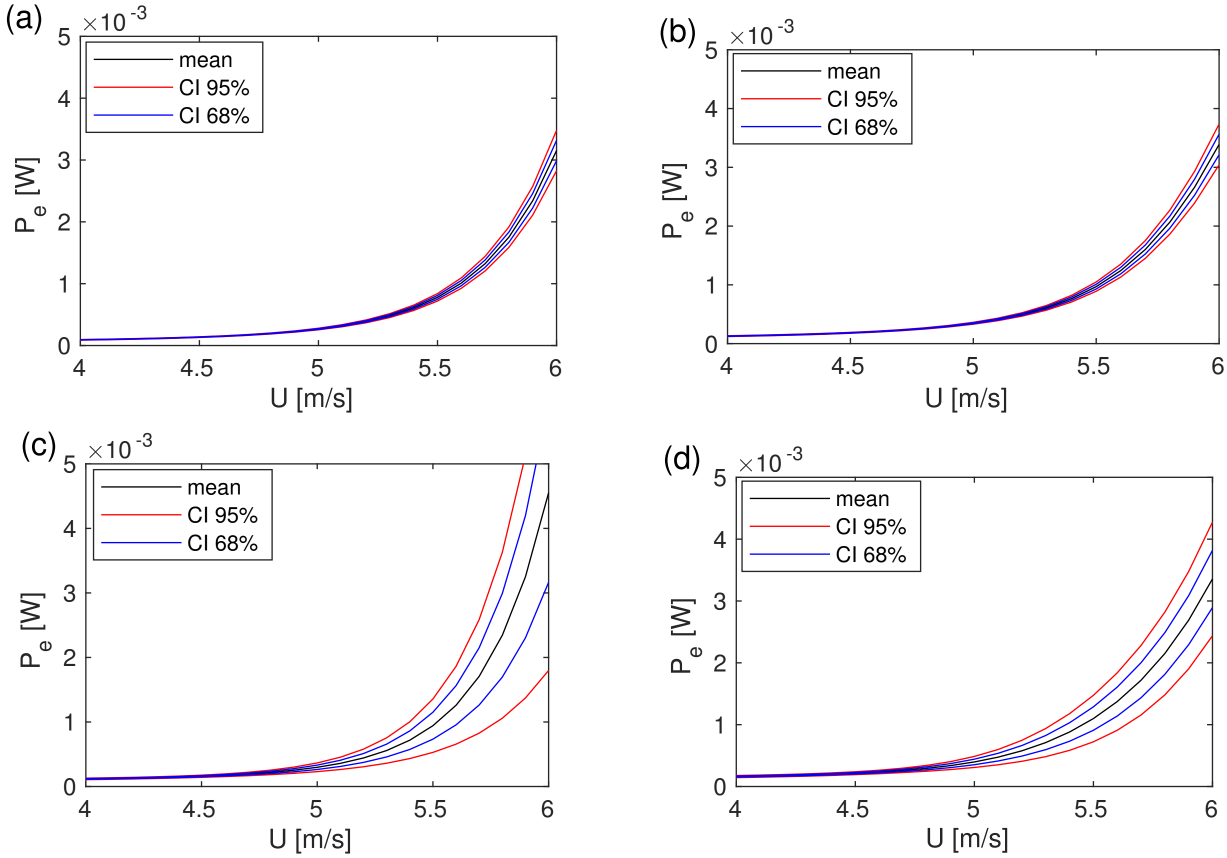

Figure 6.11: Confidence interval (CI), a) Case III with $\lambda_i = 5\%$, b) Case IV with $\lambda_i = 5\%$, c) Case III with $\lambda_i = 15\%$ and d) Case IV with $\lambda_i = 15\%$.

Chapter 7

Conclusions and Contributions

This chapter shows conclusions of the thesis and contributions.

7.1 Conclusions

This work provides an analysis of the PNES aeroelastic energy harvesting system in flutter condition, combining analytical methods, numerical simulations and probabilistic approaches. The main conclusions are described below:

- In chapter 4, three aerodynamic models (Edwards, Dimitriadis and Dowell) are compared. The Dowell model predicts a lower flutter velocity (U^*) compared to the Edwards and Dimitriadis models, while maintaining the same qualitative trend. For the remainder of this work, the Dowell model is adopted due to its analytical simplicity and high relevance in the literature concerning aeroelastic typical sections with Nonlinear Energy Sinks (NES).
- The LOM-Dowell model correctly captures the trend of increasing flutter velocity (U^*) as a function of the cubic nonlinear stiffness (δ) and shows good agreement in the system's resonance frequency in comparison to multibody-CFD model. The multibody-CFD model predicts a significantly higher U^* and reveals complex aerodynamic phenomena and a non-zero moment, underscoring that while

the LOM-Dowell model is efficient for parametric analysis, complex physics demand more complex simulations, such as multibody-CFD model. In summary, LOM-Dowell model is validated against a multibody-CFD model, confirming the LOM-Dowell model's suitability for capturing key aeroelastic trends and providing a more tractable and less demanding framework for the subsequent parametric and probabilistic analyses.

- The analytical results obtained using the Multiple Scales Method (MMS) for determining the amplitude of the limit cycle and the Hopf bifurcation point are validated by the numerical results obtained from the Runge-Kutta (RK) method. The term δ increases directly flutter velocity (U^*), but reduces the amplitude and, consequently, decreases the harvested electrical power (P_e). The quadratic nonlinear coupling (K) is the primary driver of energy harvesting performance. Increasing K demonstrates the ability to significantly boost the harvested electrical power (P_e) with comparatively less negative impact on stability (U^*). The design that maximizes energy harvesting performance requires a high value of K and the lowest feasible value of δ, highlighting the need to balance aerodynamic stability with energy conversion efficiency. Among all electrical parameters, the linear piezoelectric coupling (θ) is confirmed as the most influential factor, being directly proportional to P_e and inversely proportional to U^*.
- The final chapter presents a comprehensive dynamics and robustness analysis of an aeroelastic system featuring a Piezoelectric Nonlinear Energy Sink (PNES) operating at flutter conditions. The initial deterministic study reveals the complex influence of system parameters, suggesting that while the PNES enhances robustness against variations in passive electrical components (R and C_p), it maintains high sensitivity to the key electromechanical coupling parameter (θ). This finding underscores the limitations of traditional, single-parameter sensitivity methods for accurately assessing the stability of this system.

- A formal uncertainty analysis is conducted using a Monte Carlo simulation. This probabilistic approach definitively establishes the superior robustness of the nonlinear PNES system (Case IV) compared to the linear configuration (Case III). The primary finding is that while both systems perform comparably at low input uncertainty ($\lambda_i = 5\%$), the nonlinear system is significantly more robust at a high uncertainty level ($\lambda_i = 15\%$), as evidenced by the consistently lower coefficient of variation (λ_o) in its harvested power output. Furthermore, the uncertainty analysis corroborates deterministic findings regarding parameter influence: the electromechanical coupling coefficient (θ) and the plunge stiffness (k_h) are consistently identified as the most dominant parameters, showing the strongest positive and negative correlations with harvested power, respectively. Finally, the analysis of the output distribution for the nonlinear system reveals a highly asymmetrical distribution at high uncertainty, which is driven by a small number of high-power harvesting events (outliers). The subsequent analysis confirmes that these extreme events are a characteristic feature of the PNES's efficient Targeted Energy Transfer (TET) mechanism operating under high parametric variability. In conclusion, this work validates the use of uncertainty quantification for flutter-based harvesters and confirms that the inclusion of a PNES not only enables energy harvesting but also significantly enhances the system's robustness against parametric uncertainty, leading to a more reliable and stable power output than a purely linear configuration.

7.2 Contributions

The topics below show the conferences and published papers:

- Amaral, A. C. G., Silveira, M. , Multiple scales analysis of energy harvesting in aeroelastic system in flutter condition. In: XLII CILAMCE, 2021, Rio de Janeiro. Proceedings of the Ibero-Latin American Congress on Computational Methods in

Engineering, 2021.

- Amaral, A. C. G., Silveira, M. , Cubic nonlinear stiffness and quadratic nonlinear piezoelectrical coupling on the dynamic behaviour of an aeroelastic energy harvesting system. In: XLIII CILAMCE, 2022, Foz do Iguaçu. Proceedings of the Ibero-Latin American Congress on Computational Methods in Engineering, 2022.
- Amaral, A. C. G., De Marqui Jr, C., and Silveira, M. Aeroelastic energy harvesting in flutter condition increases with combined nonlinear stiffness and nonlinear piezoelectrical coupling. Journal of the Brazilian Society of Mechanical Sciences and Engineering, 45(2):111, 2023.

7.3 Future works

Based on the findings of this study, the following directions are suggested for future research:

- Multiphysics coupling: a progression of this research involves the implementation of a fully coupled multiphysics framework. Future studies should focus on integrating CFD with flexible multibody dynamics and piezoelectric constitutive models. Furthermore, incorporating the piezoelectric effect into this coupled environment is essential to evaluate the potential for aeroelastic energy harvesting.
- Uncertainty analysis: a critical next step for the consolidation of this research is the precise delimitation and characterization of individual parameter values. Future efforts should focus on a systematic parametric sensitivity analysis to isolate the influence of each parameter on the overall system response. By employing rigorous Parameter Identification (PI) techniques and experimental bench testing, it will be possible to define the exact operating ranges and confidence intervals for every input variable.

- Experimental validation in wind tunnel: To bridge the gap between numerical simulations and physical behaviour, an experimental validation campaign is proposed. This involves the construction of a physical prototype integrated with piezoelectric transducers for testing within a wind tunnel environment.

Bibliography

A. Abdelkefi, M. R. Hajj, and A. H. Nayfeh. Piezoelectric energy harvesting from transverse galloping of bluff bodies. *Smart Materials and Structures*, 22(1):015014, 2012a.

A. Abdelkefi, A. H. Nayfeh, and M. R. Hajj. Effects of nonlinear piezoelectric coupling on energy harvesters under direct excitation. *Nonlinear Dynamics*, 67(2):1221–1232, 2012b.

A. Abdelkefi, A. H. Nayfeh, and M. R. Hajj. Global nonlinear distributed-parameter model of parametrically excited piezoelectric energy harvesters. *Nonlinear Dynamics*, 67(2):1147–1160, 2012c.

A. Abdelkefi, A. H. Nayfeh, and M. R. Hajj. Modeling and analysis of piezoaeroelastic energy harvesters. *Nonlinear Dynamics*, 67(2):925–939, 2012d.

A. C. G. Amaral, C. De Marqui Jr, and M. Silveira. Aeroelastic energy harvesting in flutter condition increases with combined nonlinear stiffness and nonlinear piezoelectrical coupling. *Journal of the Brazilian Society of Mechanical Sciences and Engineering*, 45(2):111, 2023.

A. C. G. Amaral, W. De Roeck, and M. Silveira. Numerical investigation of the aeroelastic response of a naca0012-profile in flutter condition including cubic nonlinear stiffness using urans based simulations. In *Proceedings of ISMA*, pages 2203–2212, 2024.

David AW Barton, Stephen G Burrow, and Lindsay R Clare. Energy harvesting from vibrations with a nonlinear oscillator. 2010.

A. Bibo and M. F. Daqaq. Energy harvesting under combined aerodynamic and base excitations. *Journal of sound and vibration*, 332(20):5086–5102, 2013.

Y. Bichiou, M. R Hajj, and A. H. Nayfeh. Effectiveness of a nonlinear energy sink in the control of an aeroelastic system. *Nonlinear Dynamics*, 86(4):2161–2177, 2016.

E. Boroson, S. Missoum, P. Mattei, and C. Vergez. Optimization under uncertainty of parallel nonlinear energy sinks. *Journal of Sound and Vibration*, 394:451–464, 2017.

C. Covaci and A. Gontean. Piezoelectric energy harvesting solutions: A review. *Sensors*, 20(12):3512, 2020.

R. C. Dash, N. Sharma, D. K. Maiti, and B. N. Singh. Uncertainty analysis of galloping based piezoelectric energy harvester system using polynomial neural network. *Journal of Intelligent Material Systems and Structures*, 33(16):2019–2032, 2022.

A. Desai and S. Sarkar. Analysis of a nonlinear aeroelastic system with parametric uncertainties using polynomial chaos expansion. *Mathematical Problems in Engineering*, 2010(1):379472, 2010.

G. Dimitriadis. *Introduction to Nonlinear Aeroelasticity*, volume 1. John Wiley & Sons, 2017.

H. Ding and L. Q. Chen. Designs, analysis, and applications of nonlinear energy sinks. *Nonlinear Dynamics*, 100(4):3061–3107, 2020.

E. H. Dowell, H. C. Curtiss, R. H. Scanlan, and F. Sisto. *A modern course in aeroelasticity*, volume 3. Springer, 1989.

J. W. Edwards. Unsteady aerodynamic modeling for arbitrary motions. *The American Institute of Aeronautics and Astronautics*, 17:365–374, 1979.

M. Ericka, D. Vasic, F. Costa, G. Poulin, and S. Tliba. Energy harvesting from vibration using a piezoelectric membrane. In *Journal de Physique IV (Proceedings)*, volume 128, pages 187–193. EDP sciences, 2005.

A. Erturk and D. J. Inman. *Piezoelectric energy harvesting*. John Wiley & Sons, 2011.

O. V. Gendelman. Targeted energy transfer in systems with external and self-excitation. *Proceedings of the Institution of Mechanical Engineers, Part C: Journal of Mechanical Engineering Science*, 225(9):2007–2043, 2011.

M. Ghommem, A. H. Nayfeh, and M. R. Hajj. Control of limit cycle oscillations of a two-dimensional aeroelastic system. *Mathematical Problems in Engineering*, 2010, 2010.

A. Harb. Energy harvesting: State-of-the-art. *Renewable Energy*, 36:2641–2654, 2011.

D. Hartog and J. Pieter. *Mechanical vibrations*. Courier Corporation, 1985.

X. Jiang, D. M. McFarland, L. A. Bergman, and A. F. Vakakis. Steady state passive nonlinear energy pumping in coupled oscillators: theoretical and experimental results. *Nonlinear Dynamics*, 33(1):87–102, 2003.

E. Jonsson, C. Riso, C. A. Lupp, C. E. S. Cesnik, J. Martins, and B. I. Epureanu. Flutter and post-flutter constraints in aircraft design optimization. *Progress in Aerospace Sciences*, 2019.

H. Jung and S. Lee. The experimental validation of a new energy harvesting system based on the wakegalloping phenomenon. *Smart Materials and Structures*, 20(5): 055022, 2011.

M. G. Kang, W. S. Jung, C. Y. Kang, and S. J. Yoon. Recent progress on pzt based piezoelectric energy harvesting technologies. In *Actuators*, volume 5, page 5. Multidisciplinary Digital Publishing Institute, 2016.

X. Kang, J. Tang, G. Xia, J. Wei, F. Zhang, and Z. Sheng. Design, optimization, and application of nonlinear energy sink in energy harvesting device. *International Journal of Energy Research*, 2024(1):2811428, 2024.

I. Kovacic and M. J. Brennan. Forced harmonic vibration of an asymmetric duffing oscillator. *The Duffing equation: nonlinear oscillators and their behaviour*, pages 277–322, 2011.

Y. S. Lee, G. Kerschen, D. M. McFarland, W. J. Hill, C. Nichkawde, T. W. Strganac, L. A. Bergman, and A. F. Vakakis. Suppressing aeroelastic instability using broadband passive targeted energy transfers, part 2: experiments. *AIAA Journal*, 45(10):2391–2400, 2007a.

Y. S. Lee, A. F. Vakakis, L. A. Bergman, D. M. McFarland, and G. Kerschen. Suppression aeroelastic instability using broadband passive targeted energy transfers, part 1: Theory. *AIAA Journal*, 45(3):693–711, 2007b.

Y. S. Lee, A. F. Vakakis, L. A. Bergman, D. M. McFarland, and G. Kerschen. Enhancing the robustness of aeroelastic instability suppression using multi-degree-of-freedom nonlinear energy sinks. *AIAA journal*, 46(6):1371–1394, 2008a.

Y. S. Lee, A. F. Vakakis, L. A. Bergman, D. M. McFarland, G. Kerschen, F. Nucera, S. Tsakirtzis, and P. N. Panagopoulos. Passive non-linear targeted energy transfer and its applications to vibration absorption: a review. *Proceedings of the Institution of Mechanical Engineers, Part K: Journal of Multi-body Dynamics*, 222(2):77–134, 2008b.

Z. Li, S. Zhou, and Z. Yang. Recent progress on flutter-based wind energy harvesting. *International Journal of Mechanical System Dynamics*, 2(1):82–98, 2022.

R. Lifshitz and M. C. Cross. Nonlinear dynamics of nanomechanical and micromechanical resonators. *Reviews of nonlinear dynamics and complexity*, 1(1):1–52, 2008.

C. Marqui Jr and A. Erturk. Electroaeroelastic analysis of airfoil-based wind energy harvesting using piezoelectric transduction and electromagnetic induction. *Journal of Intelligent Material Systems and Structures*, 24:846–854, 2013.

C. Marqui Jr, D. C. Rebolho, E. M. Belo, and F. D. Marques. Identification of flutter parameters for a wing model. *Journal of the Brazilian Society of Mechanical Sciences*, 28, 2006.

E. M. Marqui Jr, C. Belo and F. D. Marques. A flutter suppression active controller. *Proceedings of the Institution of Mechanical Engineers, Part G: Journal of Aerospace Engineering*, 219(1):19–33, 2005.

A. H. Nayfeh and B. Balachandran. *Applied nonlinear dynamics: analytical, computational, and experimental methods*. John Wiley & Sons, 2008.

A. H. Nayfeh and A. E. S. Jebril. The response of two-degree-of-freedom systems with quadratic and cubic non-linearities to multifrequency parametric excitations. *Journal of Sound and Vibration*, 115(1):83–101, 1987.

Ali H Nayfeh and Dean T Mook. *Nonlinear oscillations*. John Wiley & Sons, 2008.

S. A. Nayfeh and A. H. Nayfeh. Energy transfer from high-to low-frequency modes in a flexible structure via modulation. 1994.

C. E Papadopoulos and H. Yeung. Uncertainty estimation and monte carlo simulation method. *Flow Measurement and Instrumentation*, 12(4):291–298, 2001.

E. Papatheou, X. Wei, S. Jiffri, M. Prandina, M. G. Tehrani, S. Bode, K. V. Singh, J. E. Mottershead, and J. E. Cooper. Flutter control using vibration test data: theory, rig design and preliminary results. In *25th International Conference on Noise and Vibration engineering, ISMA2012 in conjunction with the 4th International Conference on Uncertainty in Structural Dynamics, USD 2012*, pages 3047–3060. Katholieke Universiteit Leuven & afdeling Orthopedagogiek, 2012.

F. I. Petrescu, A. Apicella, R. V. Petrescu, S. Kozaitis, R. Bucinell, R. Aversa, and T. Abu-Lebdeh. Environmental protection through nuclear energy. *American Journal of Applied Sciences*, 13(9):941–946, 2016.

S. S. Rao and F. F. Yap. *Mechanical vibrations*, volume 4. Prentice hall Upper Saddle River, 2011.

A. Reggio and M. De Angelis. Modelling and identification of structures with rate-independent linear damping. *Meccanica*, 50(3):617–632, 2015.

R. Y. Rubinstein and D. P. Kroese. *Simulation and the Monte Carlo method*. John Wiley & Sons, 2016.

M. Safaei, H. A. Sodano, and S. R. Anton. A review of energy harvesting using piezoelectric materials: state-of-the-art a decade later (2008–2018). *Smart Materials and Structures*, 28(11):113001, 2019.

T. M. Silva, M. A. Clementino, C. Marqui Jr, and A. Erturk. An experimentally validated piezoelectric nonlinear energy sink for wideband vibration attenuation. *Journal of Sound and Vibration*, 437:68–78, 2018.

V. C. Sousa, T. M. P. Silva, and C. Marqui Jr. Aeroelastic flutter enhancement by exploiting the combined use of shape memory alloys and nonlinear piezoelectric circuits. *Journal of sound and vibration*, 407:46–62, 2017.

S. C. Stanton, A. Erturk, B. P. Mann, and D. J. Inman. Nonlinear piezoelectricity in electroelastic energy harvesters: modeling and experimental identification. *Journal of Applied Physics*, 108(7):074903, 2010a.

S. C. Stanton, A. Erturk, B. P. Mann, and D. J. Inman. Resonant manifestation of intrinsic nonlinearity within electroelastic micropower generators. *Applied Physics Letters*, 97(25):254101, 2010b.

N. G. Stephen. On energy harvesting from ambient vibration. *Journal of sound and vibration*, 293(1-2):409–425, 2006.

W. Tian, Y. Li, P. Li, Z. Yang, and T. Zhao. Passive control of nonlinear aeroelasticity in hypersonic 3-d wing with a nonlinear energy sink. *Journal of Sound and Vibration*, 462:114942, 2019.

A. Triplett and D. D. Quinn. The effect of non-linear piezoelectric coupling on vibration-based energy harvesting. *Journal of Intelligent Material Systems and Structures*, 20 (16):1959–1967, 2009.

N. Tsushima and W. Su. Flutter suppression for highly flexible wings using passive and active piezoelectric effects. *Aerospace Science and Technology*, 65:78–89, 2017.

O. Tylén. Fluid-structure interaction; stiffness effects on airfoil flutter: A numerical study of airfoil flutter in star-ccm+. 2022.

A. F. Vakakis, O. V. Gendelman, L. A. Bergman, D. M. McFarland, G. Kerschen, and Y. S. Lee. *Nonlinear targeted energy transfer in mechanical and structural systems.* Springer, 2009.

R. Viguié, G. Kerschen, and M. Ruzzene. Exploration of nonlinear shunting strategies as effective vibration absorbers. In *Active and Passive Smart Structures and Integrated Systems 2009*, volume 7288, pages 812–821. SPIE, 2009.

X. Q. Wang, Y. Liao, and M. P. Mignolet. Uncertainty analysis of piezoelectric vibration energy harvesters using a finite element level-based maximum entropy approach. *ASCE-ASME Journal of Risk and Uncertainty in Engineering Systems, Part B: Mechanical Engineering*, 7(1):010906, 2021.

C. Wei and X. Jing. A comprehensive review on vibration energy harvesting: Modelling and realization. *Renewable and Sustainable Energy Reviews*, 74:1–18, 2017.

Z. Yang, A. Erturk, and J. Zu. On the efficiency of piezoelectric energy harvesters. *Extreme Mechanics Letters*, 15:26–37, 2017.

Z. G. Ying, Y. Q. Ni, and J. M. Ko. Semi-active optimal control of linearized systems with multi-degree of freedom and application. *Journal of Sound and Vibration*, 279 (1-2):373–388, 2005.

H. Zhang, Z. Li, Z. Yang, and S. Zhou. Flutter suppression of an airfoil using a nonlinear energy sink combined with a piezoelectric energy harvester. *Communications in Nonlinear Science and Numerical Simulation*, 125:107350, 2023.

L. B. Zhang, A. Abdelkefi, H. L. Dai, R. Naseer, and L. Wang. Design and experimental analysis of broadband energy harvesting from vortex-induced vibrations. *Journal of Sound and Vibration*, 408:210–219, 2017a.

W. Zhang, Y. Liu, S. Cao, J. Chen, Z. Zhang, and J. Zhang. Targeted energy transfer between 2-d wing and nonlinear energy sinks and their dynamic behaviors. *Nonlinear Dynamics*, 90(3):1841–1850, 2017b.

W. Zhang, J. Fang, Y. He, and J. Zhang. Resonance capture and targeted energy transfer for suppressing aeroelastic instability of 2-d wing. *The European Physical Journal Special Topics*, 228(9):1873–1889, 2019.

Y. Zhang, L. Tang, and K. Liu. Piezoelectric energy harvesting with a nonlinear energy sink. *Journal of Intelligent Material Systems and Structures*, 28(3):307–322, 2017c.

X. Zheng, L. He, S. Wang, X. Liu, R. Liu, and G. Cheng. A review of piezoelectric energy harvesters for harvesting wind energy. *Sensors and Actuators A: Physical*, 352:114190, 2023.

Y. Zheng and Y. Wang. Flutter stability analysis of aeroelastic systems with consideration of hybrid uncertain parameters. *Mechanical Systems and Signal Processing*, 185: 109782, 2023.